



HORIZON EUROPE PROGRAMME – TOPIC HORIZON-CL5-2021-D3-03-05

*Wind energy in the natural and social environment
Research and Innovation action (RIA)*



wimby
WIND IN MY BACKYARD

WIMBY

Wind in My Backyard: Using holistic modelling tools to advance social awareness and engagement on large wind power installations in the EU

Grant Agreement No. 101083460

Starting date: 1st January 2023 – Duration: 36 months

Deliverable D2.4

Maps of health and safety impact metrics (b)

DOCUMENT INFORMATION

Deliverable number	D2.4
Deliverable title	Maps of health and safety impact metrics (b)
Work Package	WP2
Deliverable type	Data
Dissemination level	Public
Due date	31.12.2024/ Extended 15.04.2025
Pages	90
Document version	4.0
Lead author(s)	Romain Sacchi, Peter Burgherr (PSI), Luis Ramirez Camargo, Hsing-Hsuan Chen (UU)
Contributors	Rebecca Hueting, Anna Giulia Vicario (DBL)

The WIMBY project has received funding from the European Union’s research and innovation programme Horizon Europe under the grant agreement No. 101083460. This document reflects only the author’s view, and the Commission is not responsible for any use that may be made of the information it contains.



DOCUMENT CHANGE HISTORY

Version	Date	Author	Description
DRAFT			
0.1	01.12.2024	Romain Sacchi, PSI	Creation
FIRST PEER REVIEW			
1.0	14.02.2025	Luis Ramirez Camargo, UU	Proofreading and peer review of the noise model (draft 0.1)
1.1	19.02.2025	Romain Sacchi, PSI	Correction of noise section completed.
1.2	28.02.2025	Hsing-Hsuan Chen, UU Luis Ramirez Camargo, UU	Shadow flicker section completed.
1.3	07.04.2025	Peter Burgherr, Romain Sacchi, PSI	Addition of content (accident risk assessment), Update of Conclusions and Executive summary
SECOND PEER REVIEW			
2.0	10.04.2025	Hsing-Hsuan Chen, Luis Ramirez Camargo, UU	Reviewed version
2.1	11.04.2025	Peter Burgherr, Romain Sacchi, PSI	Comments integrated
2.2	15.04.2025	Rebecca Hueting, Anna Giulia Vicario (DBL)	Reviewed version, no comments
COORDINATOR APPROVAL			
3.0	15.04.2025	Stella Arapoglou (VUB)	Format, final review
FINAL VERSION			
4.0	15.04.2025	Stella Arapoglou (VUB)	Finalization to pdf



SHORT ABSTRACT FOR DISSEMINATION PURPOSES

Abstract

This deliverable enhances tools for evaluating wind turbine deployment's health and safety impacts across Europe, focusing on noise emissions, shadow flicker, and risk assessment. Compared to deliverable D2.3, changes in noise modelling now include the formulation of noise propagation according to ISO 9613-2:2024 standards, improved attenuation modelling (which considers attenuation caused by atmospheric conditions, ground types, and natural barriers), and the incorporation of ambient noise sources. These updates enable more accurate and region-specific assessments of turbine noise impacts.

The upgraded shadow flicker tool significantly enhances realism by integrating turbine operational periods based on wind speed, improving penumbra calculations, and incorporating terrain awareness. Validated through comprehensive comparisons with established industry software, it provides a more accurate representation of shadow flicker impacts, facilitating better site selection and enhancing the quality of information offered to users in the WIMBY interactive map.

Finally, the accident risk assessment for European wind farms provides detailed risk indicators at the NUTS2 level. Furthermore, a novel method for calculating Disability-Adjusted Life Years (DALY) has been developed, integrating various health impacts (i.e., fatalities and injuries) that can be included in the WIMBY interactive map. Data-based risk indicators can help clarify the controversial discussions on subjective risk perception and the general acceptance of wind power. Risk indicators at the NUTS2 level show substantial variability between and within countries. The EU, UK, and EFTA countries perform better than the OECD group, while EU candidate countries remain much closer to the non-OECD country group, except for Turkey.

Together, these advancements improve the functionality of the WIMBY's interactive map and offer users enhanced information about the potential impacts of a simulated wind farm case.



TABLE OF CONTENTS

1. Objectives and Context.....	16
1.1 Structure of the Report	17
2. Noise Impact Assessment	19
2.1 Progress since the first version (D2.3).....	19
2.1.1 Geometric divergence (<i>A_{div}</i>).....	21
2.1.2 Atmospheric attenuation	21
2.1.3 Ground and barrier attenuation (<i>A_{gr}</i> + <i>A_{bar}</i>).....	24
2.1.3.1 Ground Attenuation Calculation (<i>A_{gr}</i>).....	24
2.1.3.1.1 Elevation Data Retrieval	24
2.1.3.1.2 Distance Calculations	25
2.1.3.1.3 Ground Profile Analysis	26
2.1.3.2 Barrier attenuation (<i>A_{bar}</i>).....	27
2.1.3.3 Aggregation	28
2.1.4 Terms aggregation.....	28
2.1.5 <i>L_{den}</i>	29
2.1.6 Ambient noise sources	32
2.1.7 Examples	33
2.1.8 Human settlements.....	37
2.2 EU maps of potential noise impacts	37
2.3 Validation.....	40
2.4 Calculation time	41
3. Shadow flicker tool.....	42
3.1 Tool improvement from version a.....	42
3.1.1 Including wind condition in shadow flicker tool	42
3.1.2 Improving the shadow geometry calculation.....	43
3.1.3 Shadow flicker accounting for topography.....	52
3.1.4 Shadow geometry transformation on topography.....	52
B) Viewshed application.....	57
3.1.5 Visualization	61
4. Accident risk assessment.....	65
4.1 Updates and extensions since the intermediate version.....	65
4.2 Overview of methodological approach	66
4.2.1 Update of accidents database.....	66
4.2.2 Calculation of risk indicators	67










4.2.3	Calculation of DALY and risk map.....	68
4.3	Results	76
4.3.1	Risk indicators.....	76
4.3.2	DALY risk map.....	82
5.	Conclusions	85
REFERENCES	87



LIST OF PARTNERS

No	Logo	Name	Short Name	Country
1		VRIJE UNIVERSITEIT BRUSSEL	VUB	Belgium
2		DANMARKS TEKNISKE UNIVERSITET	DTU	Denmark
3		INTERNATIONALES INSTITUT FUER ANGEWANDTE SYSTEMANALYSE	IIASA	Austria
4		UNIVERSITAET FUER BODENKULTUR WIEN	BOKU	Austria
5		UNIVERSITETET I OSLO	UiO	Norway
6		NAZKA MAPPS BVBA	NAZKA	Belgium
7		KELSO INSTITUTE EUROPE GEMEINNUTZIGE GMBH	KIE	Germany
8		DEEP BLUE SRL	DEEP BLUE	Italy
9		UNIVERSITEIT UTRECHT	UU	Netherlands
10		POLITECNICO DI TORINO	POLITO	Italy
11		UNIVERSITA DEGLI STUDI DI PALERMO	UNIPA	Italy
12		APREN-ASSOCIACAO PORTUGUESA DE ENERGIAS RENOVAVEIS	APREN	Portugal
13		MULTICONSULT NORGE AS	MCN	Norway
14		EIDGENOESSISCHE TECHNISCHE HOCHSCHULE ZUERICH	ETH Zürich	Switzerland
15		PAUL SCHERRER INSTITUT	PSI	Switzerland
16		UNIVERSITY COLLEGE LONDON	UCL	United Kingdom

ABBREVIATIONS

Acronym	Description
COP	Conference of the Parties
dB	decibel
dB(A)	A-weighted decibel
ENSAD	ENergy-related Severe Accident Database
EPSG	European Petroleum Survey Group Geodesy
GIS	Geographic information system
GW	Gigawatt
GWe-yr	Gigawatt-electric-year
kb	Kilobytes
LCA	Life-cycle Assessment
L_{den}	Noise level day-evening-night
Mb	Mega-bytes
NGO	Non-Governmental Organization
NLP	Natural Language Processing
NUTS	Nomenclature of Territorial Units for Statistics
OECD	Organisation for Economic Co-operation and Development
SaS	Scotland against Spin
SF	Shadow flicker
WHO	World Health Organisation

LIST OF FIGURES

Figure 1 Geometric divergence sound attenuation with a noise sound located at 43°27'50.6"N 5°13'52.1"E (near Marseille, France). X and Y axes represent the distance from the noise emission source point.....21

Figure 2 Atmospheric sound attenuation with a noise sound located at 43°27'50.6"N 5°13'52.1"E (near Marseille, France) for different atmospheric conditions. X and Y axes represent the distance from the noise emission source point. 24

Figure 3 a) Aerial view of a hypothetical wind turbine located at 43°27'50.6"N 5°13'52.1"E (near Marseille, France). b) Corresponding ground elevation profile. The vertical red bar represents the wind turbine location, with a hub height of 65 m. 25

Figure 4 Sound attenuation due to the ground surface for a noise source located at 43°27'50.6"N 5°13'52.1"E.27

Figure 5 Sound attenuation due to the terrain obstacles and barriers for a 2.5 MW wind turbine with a hub height of 70 meters, located at 43°27'50.6"N 5°13'52.1"E..... 28

Figure 6 Incremental application of sound attenuation terms on a 2.5 MW wind turbine with a sound power at the source of 108 dB(A), located at 43°27'50.6"N 5°13'52.1"E. **LW**: sound power level of the source. **Adiv**: sound attenuation due to geometric divergence. **Aatm**: sound attenuation due to atmospheric absorption. **Agr**: sound attenuation due to ground surface interference. **Abar**: sound attenuation due to terrain obstacles and barriers. 29

Figure 7 L_{den} noise emissions of a hypothetical 2.5 MW wind turbine $L_{den(wind)}$, in dB(A), near the village of Sacerno, northeast of the Bologna Airport. Background map: OpenStreetMap..... 34

Figure 8 Existing L_{den} noise emissions $L_{den(amb)}$, in dB(A), in Sacerno, northeast of Bologna Airport, identified using European Noise maps data. Background map: OpenStreetMap..... 35

Figure 9 Overall L_{den} noise emissions $L_{den(total)}$, in dB(A), in Sacerno, northeast of Bologna Airport, considering existing noise sources from the Bologna airport, as well as those from the hypothetical wind turbine. Background map: OpenStreetMap..... 35

Figure 10 Net contribution to L_{den} noise emission levels $L_{den(net)}$, in dB(A), of a hypothetical 2.5 MW wind turbine in Sacerno, northeast of Bologna Airport.

Only a limited area northeast of Sacerno sees its exposure to noise levels increase by 30 to 39 dB(A). Background map: OpenStreetMap..... 36

Figure 11 L_{den} noise emission levels of a hypothetical 5 MW wind turbine $L_{den(wind)}$, located at 43°32'14.4"N 5°41'19.9"E, between two ridges of the Sainte-Victoire mountain, overlooking the village of Puyloubier, France. Background map: OpenStreetMap.....37

Figure 12 Screen capture of the map showing characterisation of net L_{den} contribution of currently operating wind turbines in Europe. The EU Commission sets the recommended maximum noise level exposure at $L_{den} = 55 \text{ db(A)}$ 39

Figure 13 Close-up view on Sakskøbing, Denmark, shows wind turbines' net L_{den} contribution. 39

Figure 14 Illustration of the shadow penumbra at the edge of a wind turbine's full shadow..... 45

Figure 15 a) The new SF_tool result, with corrected shadow geometry. b) The shadow flicker results from the previous version of SF_tool, taking turbine geometry as shadow geometry..... 47

Figure 16 The updated SF tool result in the Netherlands (yellow to dark blue area) compared to the WindPRO result at the same location (52.902449, 5.852967.) 48

Figure 17 The highest overlapping case. The turbine geometry is shown as a light blue circle at (50.000408, 5.852967). The green area represents the shadow flicker coverage region greater than 30 hours/year simulated by WindPRO; the pink area represents the coverage area greater than 30 hours/year modelled by SF_tool. The topography contour map only contains the contour line up to 50 meters (in black), indicating a relatively flat and homogeneous terrain. 49

Figure 18 The lowest overlapping case. The turbine geometry is shown as a light blue circle at (52.212653, 5.852967). The darker blue area represents the shadow flicker coverage region greater than 30 hours/year simulated by WindPRO; the orange area represents the coverage area greater than 30 hours/year modelled by SF_tool. The topography contour map shows the 50- and 100-meter lines (in black and brown), indicating more hilly terrain, especially on the map's northern side..... 50

Figure 19 Distribution of differences between SF_tool and WindPRO simulation for the area with >30hr/year shadow flicker impact in the Netherlands validation..... 50



Figure 20 a) Correlation between SF_tool and WindPRO for the validation in the Netherlands. This figure shows SF_tool > 30hr/year areas (y-axis), the WindPRO > 30hr/year areas (x-axis), and the regression line. b) Relative error distribution histogram between the shadow flicker simulation results (> 30hr/year area) of SF_tool and WindPRO..... 51

Figure 21 (a) and (b) represent the altitude maps, showing the vertical angles from each pixel to the turbine rotor top and bottom, respectively. (c) represents the azimuth map, which indicates the direction of each pixel relative to the turbine. (d) highlights the pixels that can be cast into shadow from the turbine rotor top, while (e) represents those cast from the turbine rotor bottom..... 55

Figure 22 (a) depicts the altitude mask, computed as the difference between the altitude maps for the turbine rotor top and bottom. This highlights the potential shadow-casting area. (b) illustrates the azimuth mask, incorporating a tolerance of 5°. (c) presents the overlapping region of (a) and (b), effectively delineating the final shadow footprint at a given time step..... 56

Figure 23 The shadow flicker map includes shadow transformation on terrains, with turbine location (50.866422, 5.852967) in the Netherlands. ... 57

Figure 24 Shadow flicker map excluding the viewshed area (in black), for turbine location (50.866122, 5.852967) in the Netherlands..... 58

Figure 25 Shadow flicker distribution in a mountainous region of Spain. The shadow flicker map (dark regions) is overlaid on an elevation map, demonstrating the influence of topography on shadow propagation. Higher elevations (red-orange) and lower areas (blue-green) affect the extent and shape of flicker exposure..... 59

Figure 26 Correlation Between SF_tool and WindPRO for validation in Spain cases..... 60

Figure 27 Distribution of differences between SF_tool and WindPRO for validation in Spain cases..... 61

Figure 28 Relative Error Distribution for validation in Spain cases..... 61

Figure 29 A final shadow flicker map in the Netherlands. The final shadow flicker map incorporating viewshed analysis and transformed shadow propagation, with shadow flicker frequency represented using a gradient colour scale..... 62

Figure 30 Contour map of shadow flicker frequency. A contour-based visualization of shadow flicker coverage, categorized into 10, 30, and 100-



hour intervals, illustrates the extent and intensity of shadow flicker exposure.
 63

Figure 31 Binary Shadow Flicker Contour Map – A simplified contour representation of shadow flicker coverage, distinguishing between areas with less than 30 hours and greater than 30 hours of shadow flicker per year with single-color bands..... 64

Figure 32: Approach to estimating Disability-Adjusted Life Years (DALY) for all accidents considered in the years 2000–2023 across European countries. YLL = Years of Life Lost, YLD = Years Lived with Disability, YAD = Years with Anxiety Disorder..... 70

Figure 33: Onshore and offshore fatality rates for all accidents (with ≥1 fatality) and severe accidents (with ≥5 fatalities) in OECD, EU27, and non-OECD countries (adapted from Burgherr et al., 2023). 77

Figure 34: Raw fatality rates at NUTS2 level for EU27, UK, EFTA, and EU candidate countries, covering the period 2000–2023. 79

Figure 35: Average severe fatality rates and confidence intervals for each country, 2000–2023. Horizontal, dashed lines indicate average values per country group..... 80

Figure 36: DALY rates (DALY = Disability-Adjusted Life Years) at the NUTS2 level for 38 European countries. NUTS2 units that feature a point pattern indicate that no DALY rates are available based on the current dataset. ... 83



LIST OF TABLES

Table 1 Root Mean Squared Error of noise level prediction, in $db(A)$. Number of data points for training = 333. Number of data points for testing: 84. 40

Table 2 CPU time for computing L_{den} noise contours for various wind turbines. CPU time (WindWhisper) = CPU time spent executing code that belongs to the WindWhisper model. CPU time (system) = CPU time spent executing code outside the WindWhisper model..... 41

Table 3 The descriptive statistics of Spain cases between SF_tool and WindPRO, considering the topography impacts in SF_tool. 60



EXECUTIVE SUMMARY

This deliverable outlines significant improvements in assessing the health and safety impacts associated with wind turbine deployment in Europe. Building on the foundations established in Deliverable D2.3, it introduces enhanced methodologies and tools for modeling noise emissions, shadow flicker, and accident risks. These advancements are essential for enabling more informed, data-driven decisions in regional planning and public engagement related to wind energy.

Noise Impact Assessment:

The updated noise propagation model utilizes the ISO 9613-2:2024 standard and includes new modules to account for ground and barrier attenuation, along with ambient noise sources. This enables users of the WIMBY interactive map to differentiate between turbine-generated noise and existing environmental noise (e.g., highways, airports), as well as to simulate region-specific scenarios with customizable meteorological conditions. By overlaying noise outputs with settlement maps and population density data, the model now allows estimates of how many individuals may be exposed to noise levels exceeding regulatory thresholds. This functionality not only aids environmental permitting processes but also fosters public trust through transparency.

Shadow Flicker Assessment:

The shadow flicker model now incorporates wind speed data to simulate turbine operation more realistically and integrates solar geometry, rotor dynamics, and terrain effects to calculate the extent and intensity of shadow flicker exposure. It also considers penumbra widening due to the sun's angular size and adjusts for obstruction caused by topography through viewshed analysis. Validation against WindPRO indicates strong agreement in both flat and complex terrains. The output is designed for intuitive communication, featuring clear binary maps that identify regions with more than 30 hours/year of shadow flicker exposure – a threshold used in several national permitting guidelines.

Accident Risk Assessment:



A novel framework quantifies wind power-related accident risks at the NUTS2 level, incorporating a comprehensive accident dataset and introducing a novel methodology for estimating Disability-Adjusted Life Years (DALY). These risk indicators are displayed through interactive maps, enabling stakeholders to grasp the distribution and severity of health impacts across regions. The framework facilitates nuanced comparisons between countries and supports evidence-informed discussions regarding wind power safety, particularly in the context of social acceptance debates.

Together, these tools significantly enhance the capacity of the WIMBY project to provide credible, high-resolution insights into the potential health and safety impacts of wind energy. They are designed to be modular, reproducible, and transparent, serving local planners, environmental agencies, and the public alike.

Next Steps:

Future work will focus on further integrating these tools into the WIMBY interactive map under WP5, expanding the geographic scope and improving impact quantification. For the noise model, this includes translating Lden metrics into DALY-based health impact indicators. For shadow flicker, efforts will explore visualization options and user interaction design to enhance public understanding. Ultimately, these developments aim to support a just and sustainable rollout of wind power by equipping stakeholders with high-quality, contextual information.



1. Objectives and Context

The WIMBY project, launched in 2023, addresses the complex challenges of wind turbine installation in Europe by incorporating advanced tools for modeling environmental and social impacts. This updated deliverable refocuses on showcasing the progress made in health and safety impact assessments since the initial report (D2.3). Specifically, this version enhances the methodologies for noise propagation modeling, shadow flicker evaluation, and accident risk mapping.

Key achievements include:

Noise Impact Assessment: The adoption of ISO 9613-2:2024 standards has significantly improved the accuracy of noise propagation models by expanding the range of attenuation factors taken into account. The new methodology, in addition to the attenuation caused by geometric divergence and atmospheric absorption, now includes ground and barrier effects, allowing for highly detailed and context-specific noise impact assessments.

Key enhancements also involve integrating European Environmental Agency noise maps to separate wind turbine noise from ambient sources, providing a more comprehensive view of total noise contributions. Consequently, the tool now accounts for ambient noise layers such as highways, railways, and industrial sources, enabling the evaluation of cumulative noise impacts.

These advancements enable a more nuanced understanding of noise impacts across various European regions, providing future WIMBY interactive map users with actionable data for sustainable wind turbine deployment. Initial validation efforts, which compared model outputs to real-world datasets, demonstrate promising reliability and will be further developed in future iterations.

Shadow flicker: The updated shadow flicker model now incorporates turbine operational downtime by integrating wind speed data, enabling more realistic projections that extend beyond worst-case assumptions. It



also improves geometric accuracy by modeling the penumbra effect caused by the sun's angular size and introduces terrain-aware projections that adapt shadow geometry based on topographical features. These advancements yield a more accurate estimation of annual shadow flicker exposure across various European landscapes, supporting better compliance with regulatory thresholds (e.g., 30 hours/year) and fostering more transparent communication with communities.

Risk Assessment Enhancements: The methodological advancements regarding risk assessment for accidents at wind farms are detailed in Chapter 4.1. In summary, these consist of four aspects:

1. Compilation of a comprehensive accident dataset based on publicly available information, offering global coverage with a specific focus on Europe.
2. The accident database has been connected to infrastructure data to provide a more location-specific approach to accident treatment.
3. The geographic resolution of results has been reduced from the typically calculated risk indicators for country groups to the NUTS2 level.
4. A novel methodology for a DALY risk indicator has been developed, allowing for the aggregate consideration of various types of health impacts (i.e., fatalities and injuries).

By implementing these enhancements, this deliverable advances the WIMBY project's overarching goal of providing robust, open-source tools that enable informed and sustainable wind energy deployment while minimizing adverse impacts on communities and ecosystems.

1.1 Structure of the Report

This report outlines the methodologies employed and the results obtained for each impact category, primarily focusing on the progress made since the previous version of the deliverable (i.e., D2.3):

- **Noise Impact Assessment:** Details the approach for modeling noise propagation and identifying affected populations.
- **Shadow Flicker Impact Assessment:** Describes the evaluation of flicker exposure in communities near wind turbines.



- Accident Risk Assessment: Highlights risks associated with operational and structural failures of wind installations.

These sections together provide a foundational understanding of the health and safety metrics relevant to wind turbine deployment and their implications for EU policy and community planning.



2. Noise Impact Assessment

The WIMBY project's noise impact assessment focuses on accurately modeling and analyzing noise propagation from wind turbines. This assessment identifies potential impacts on nearby human settlements by integrating environmental, geographic, and turbine-specific factors. The methodologies include advanced modeling of noise attenuation due to atmospheric, ground, and obstacle interactions, along with the influence of ambient noise levels and settlement distributions.

2.1 Progress since the first version (D2.3)

A notable change regarding the noise propagation estimate is the change in the standard used to calculate the different attenuation terms. We now use ISO 9613-2:2024 (International Organization for Standardization 2024), an update from the 1996 version used in the report. The content and methods presented in the updated standard do not contradict the previous version but add additional context and information, notably concerning attenuation estimation due to ground and barriers.

Section 6 of ISO 9613-2:2024 outlines the basic formulae used to calculate the sound pressure level at a receiver location, accounting for various factors that influence sound propagation outdoors. The key equation for the equivalent continuous sound pressure level ($L_{fT(DW)}$) is:

$$L_{fT(DW)} = L_W + D_c - A$$

Where:

- L_W : The sound power level of the source in decibels (relative to 1 picowatt).
- D_c : The directivity correction, which adjusts for the sound source's directionality (in dB).
- And A : The total attenuation during sound propagation, which is expressed as the sum of multiple attenuation components.

The total attenuation (A) combines several effects:

$$A = A_{div} + A_{atm} + A_{gr} + A_{bar} + A_{misc}$$



With:

- A_{div} : It accounts for spreading sound waves as they travel outward, modelled as spherical spreading.
- A_{atm} : It represents sound energy loss due to absorption by air molecules.
- A_{gr} : It reflects the effect of sound interaction with the ground surface, incorporating surface types like hard or porous ground.
- A_{bar} : It accounts for sound diffraction over or around obstacles, considering factors like barrier height and distance from the source and receiver.
- A_{misc} : It captures additional effects, such as foliage or complex terrain.

WIMBY's D2.3 described a Python library ([WindWhisper](#)) that could model the directionality of noise (D), considering geometric divergence (A_{div}) and atmospheric attenuation (A_{atm}) for a given wind turbine's sound power level (L_W).

We now describe improvements to the model, notably improvements to atmospheric attenuation modelling (A_{atm}) and the inclusion of additional attenuation terms (A_{gr} and A_{bar}). We also include existing noise sources to determine the net contribution of one or several wind turbines to the overall noise level.

Currently, the estimate of A_{misc} remains out of the tool's scope. It also excludes D_c for several reasons. First, modern wind turbines are often approximated as isotropic sound sources, especially at the distances relevant for noise impact assessments, where any minor directional variations in sound emissions tend to average out. Furthermore, attenuation factors such as geometric divergence (A_{div}), atmospheric absorption (A_{atm}), ground effects (A_{gr}), and barrier attenuation (A_{bar}) dominate the overall sound propagation, making the contribution of D_c negligible in comparison. Additionally, noise regulations and environmental standards typically emphasise A-weighted sound levels based on simplified propagation models, which do not explicitly require D_c . At greater distances from the

source, where most assessments focus, the directional effects diminish as sound waves spread more evenly, further reducing its significance.

2.1.1 Geometric divergence (A_{div})

The estimation of the attenuation of sound due to geometric divergence has not changed. It is calculated, according to ISO 9613-2:2024, as:

$$A_{div} = 20 \log_{10} \frac{d}{d_0}$$

With:

- d : the distance, in meters, between the wind turbine and the sound receiver
- d_0 : the reference distance (here, 1 m).

Figure 1 describes the sound attenuation caused by geometric divergence A_{div} on a 2'000 by 2'000 meters grid, with a noise source at 43°27'50.6"N 5°13'52.1"E.

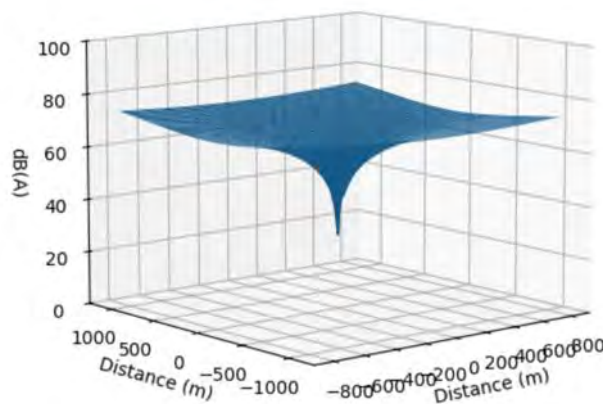


Figure 1 Geometric divergence sound attenuation with a noise sound located at 43°27'50.6"N 5°13'52.1"E (near Marseille, France). X and Y axes represent the distance from the noise emission source point.

2.1.2 Atmospheric attenuation

Atmospheric attenuation reduces the intensity of sound waves as they travel through the air. The *WindWhisper* tool implements calculations based

on ISO 9613-1 standards (ISO 2010). The key equation for atmospheric attenuation $\alpha(f)$ as a function of frequency f is:

$$\alpha(f) = A_{oxygen}(f) + A_{nitrogen}(f) + A_{humidity}(f)$$

Where:

- $A_{oxygen}(f)$: Attenuation due to oxygen absorption
- $A_{nitrogen}(f)$: Attenuation due to nitrogen absorption
- $A_{humidity}(f)$: Attenuation caused by the presence of water vapour in the air

The total attenuation over a distance d is given by:

$$L_{atm} = \alpha(f) \cdot d$$

In D.2.3, *WindWhisper* provided only one α coefficient ($\alpha = 2$), representing an environmental setting of 20 °C at 80% relative humidity. However, to better fit the regional conditions of the wind turbine (s) implementation, *WindWhisper* now provides several [α coefficients](#) (from Table 2 of ISO 9613-1) corresponding to specific temperatures (10, 15, 20, and 30 °C) and humidity (20, 50, 70, and 80%) levels.

However, these coefficients apply to third-octave bands, while the *WindWhisper* model estimates A-weighted noise emissions (dB(A)). Hence, the tool calculates a weighted absorption coefficient ($a_{weighted}$) for sound attenuation in the atmosphere by integrating the spectral energy contributions of various frequency bands with their corresponding absorption coefficients. It applies a standard ISO-based A-weighting correction ($A_{weighting}$) to account for human auditory sensitivity. Predefined spectral sound levels ($L_{spectral}$) for each frequency band are first adjusted by reversing the A-weighting corrections:

$$L_{unweighted} = L_{spectral} - A_{weighting}$$

The unweighted sound levels are then converted to energy contribution (E) using the formula:

$$E = 10^{(L_{unweighted}/10)}$$

These energy contributions are used to weight the absorption coefficients for each frequency band. The final weighted absorption coefficient is calculated as:

$$\alpha_{weighted} = \frac{\Sigma(E \times \alpha(f))}{\Sigma E}$$

This ensures that frequency bands with higher energy contributions have a proportionally more significant influence on the result. The output, expressed in dB/km, represents the effective atmospheric sound attenuation (A_{atm}), capturing the spectral distribution of sound energy and its interaction with atmospheric conditions.

When implemented in the WINBY interactive map, users can select the atmospheric conditions (i.e., average temperature and humidity levels) most appropriate for the location of the simulation, and appreciate their effects on noise emission propagation.

Figure 2 describes the sound attenuation caused by geometric divergence A_{div} on a 2'000 by 2'000 meter grid, with a noise source at 43°27'50.6"N 5°13'52.1"E. For example, with an ambient temperature of 10°C, and a relative humidity of 70%, the sound attenuation level reaches about 6 dB(A) at 1'000 meters away from the noise emission source point.

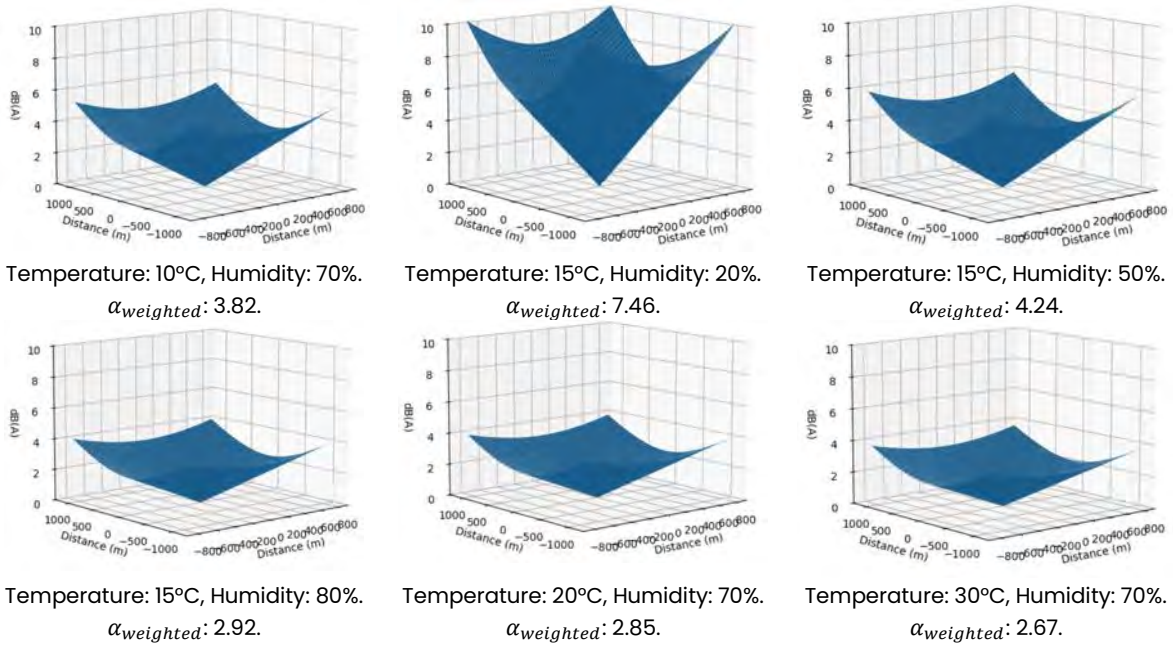


Figure 2 Atmospheric sound attenuation with a noise sound located at 43°27'50.6"N 5°13'52.1"E (near Marseille, France) for different atmospheric conditions. X and Y axes represent the distance from the noise emission source point.

2.1.3 Ground and barrier attenuation ($A_{gr} + A_{bar}$)

This section describes the methodology used to estimate noise attenuation caused by ground surface interactions and terrain obstacles or barriers based on the principles outlined in ISO 9613-2:2024. The calculations incorporate geographic, elevation, and wind turbine data to model sound propagation and attenuation effects.

2.1.3.1 Ground Attenuation Calculation (A_{gr})

As explained above, the ground attenuation component (A_{gr}) represents the impact of sound wave interaction and interference with the ground surface. The following steps outline the procedure:

2.1.3.1.1 Elevation Data Retrieval

Elevation data for the study area relies on the Copernicus DEM map, provided by the European Space Agency (ESA), with either a 30 meters or 90 meters resolution. If such resource is not available, WindWhisper can also

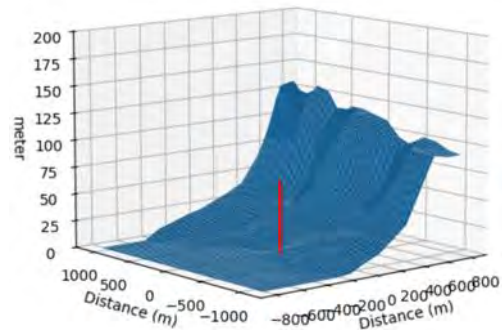


use the Open Elevation API¹. This free, open-source option, however, has strict query constraints. Non-open-source options (e.g., Google Maps) may be considered for higher performance. When the elevation data is retrieved, relative elevations are computed between wind turbine sources and receiver points on a geographic grid.

Figure 3 illustrates an aerial view of a hypothetical wind turbine situated at 43°27'50.6"N, 5°13'52.1"E (a), on a 2'000 by 2'000 meter grid. It also presents the corresponding elevation data displayed on a grid (b).



a) Aerial view (Google Maps)



b) Data retrieved from Open Elevation.

Figure 3 a) Aerial view of a hypothetical wind turbine located at 43°27'50.6"N 5°13'52.1"E (near Marseille, France). b) Corresponding ground elevation profile. The vertical red bar represents the wind turbine location, with a hub height of 65 m.

2.1.3.1.2 Distance Calculations

Haversine (horizontal) distances between sources and receivers are combined with relative elevation data to compute actual Euclidean distances (d_g) for each grid cell using:

$$d_g = \sqrt{(d_{haversine})^2 + (\Delta elevation)^2}$$

¹ <https://open-elevation.com/>

2.1.3.1.3 Ground Profile Analysis

For each sound path, a profile of elevations $h_{ground}(x)$ is interpolated along the propagation line between the source and receiver. Then, a straight-line elevation profile is computed between the source and receiver for comparison with the actual ground profile, calculated as:

$$h_{ground}(x) = h_{source} + \frac{h_{receiver} - h_{source}}{d} \cdot x$$

Where:

- $h_{ground}(x)$ represents the elevation at any point along the direct path,
- h_{source} and $h_{receiver}$ are the elevations of the source and receiver, respectively. Note that h_{source} includes the rotor hub height.
- d is the total distance between the source and receiver,
- And x is the distance from the source to a point along the path.

WindWhisper then proceeds to calculate the area (F) between the straight-line elevation and the actual ground profile:

$$F = \int_0^{d_g} (h_{straight}(x) - h_{ground}(x)) dx$$

Indeed, as F is needed to obtain the mean height of the propagation path above the ground:

$$h_m = \frac{F}{d_g}$$

Once d_g and h_m are known for each path between the wind turbine(s) and each cell of the grid, A_{gr} is obtained:

$$A_{gr} = 4.8 - \frac{2h_m}{d_g} \left(17 + \frac{300}{d_g} \right)$$

Figure 4 illustrates the sound attenuation due to the ground surface interference A_{gr} on a 3'300 by 3'300 meters grid, with a noise source at 43°27'50.6"N 5°13'52.1"E.

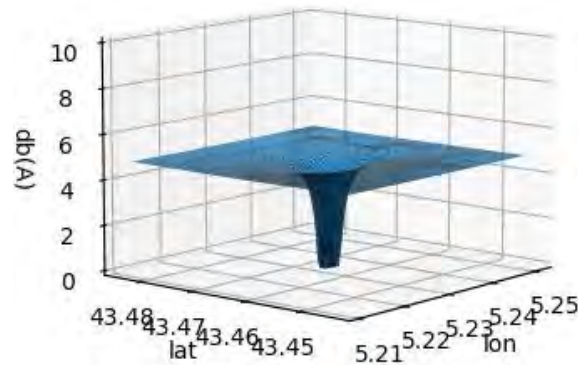


Figure 4 Sound attenuation due to the ground surface for a noise source located at 43°27'50.6"N 5°13'52.1"E.

2.1.3.2 Barrier attenuation (A_{bar})

Barrier attenuation (A_{bar}) quantifies the reduction in sound energy due to obstacles present along the propagation path between the wind turbines and the potential receiver (i.e., each grid cell). The tool's methodology follows ISO 9613-2:2024 and is detailed below.

The process begins by analyzing the elevation profile along the direct line of sight between the source and receiver. The actual terrain profile, $h_{ground}(x)$, is compared to the straight-line path, $h_{straight}(x)$. Obstacles are identified if the terrain elevation exceeds the straight-line elevation by a margin of 5 meters:

$$obstacle_{mask} = h_{path}(x) > h_{line} + \Delta$$

Where $\Delta = 5m$.

When obstacles are detected, the path length difference (z) is calculated to quantify the impact of diffraction over the obstacle. The formula for z is:

$$z = d_{SS} + d_{SR} - d$$

Where

- d_{SS} is the distance from the source to the top of the first obstacle,
- d_{SR} is the distance from the top of the obstacle to the receiver,
- and d is the total straight-line distance between the source and receiver.

This path length difference is essential for determining the amount of diffraction caused by the obstacle.

The sound attenuation due to the obstacle (A_{bar}) is computed using the ISO 9613-2 barrier attenuation formula:

$$A_{bar} = 10 \cdot \log_{10} \left(3 + 40 \cdot \frac{z}{\lambda_{eff}} \right)$$

Where:

- λ_{eff} is the effective wavelength of the sound for the A-weighted spectrum, typically set to 0.34m for a frequency of 1 kHz.

The formula models the reduction in sound intensity due to diffraction, with attenuation increasing logarithmically as the path length difference (z) grows.

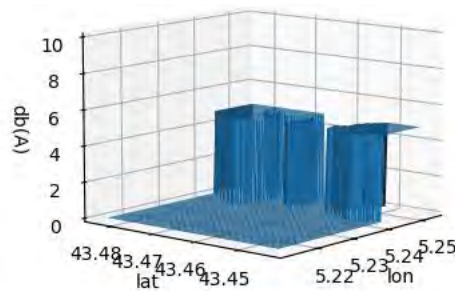


Figure 5 Sound attenuation due to the terrain obstacles and barriers for a 2.5 MW wind turbine with a hub height of 70 meters, located at 43°27'50.6"N 5°13'52.1"E.

2.1.3.3 Aggregation

A_{gr} and A_{bar} are calculated for each grid cell, with one grid per wind turbine modelled. For grid cells that are influenced by multiple turbines, A_{gr} and A_{bar} are aggregated by selecting the minimum attenuation across all turbines. This ensures that the final attenuation values reflect realistic cumulative sound levels by accounting for the least attenuated contributions.

2.1.4 Terms aggregation

Figure 6 describes the incremental application of attenuation terms on an unattenuated sound power of 108 dB(A), in order to obtain the continuous sound pressure level ($L_{FT(DW)}$) for each grid cell.

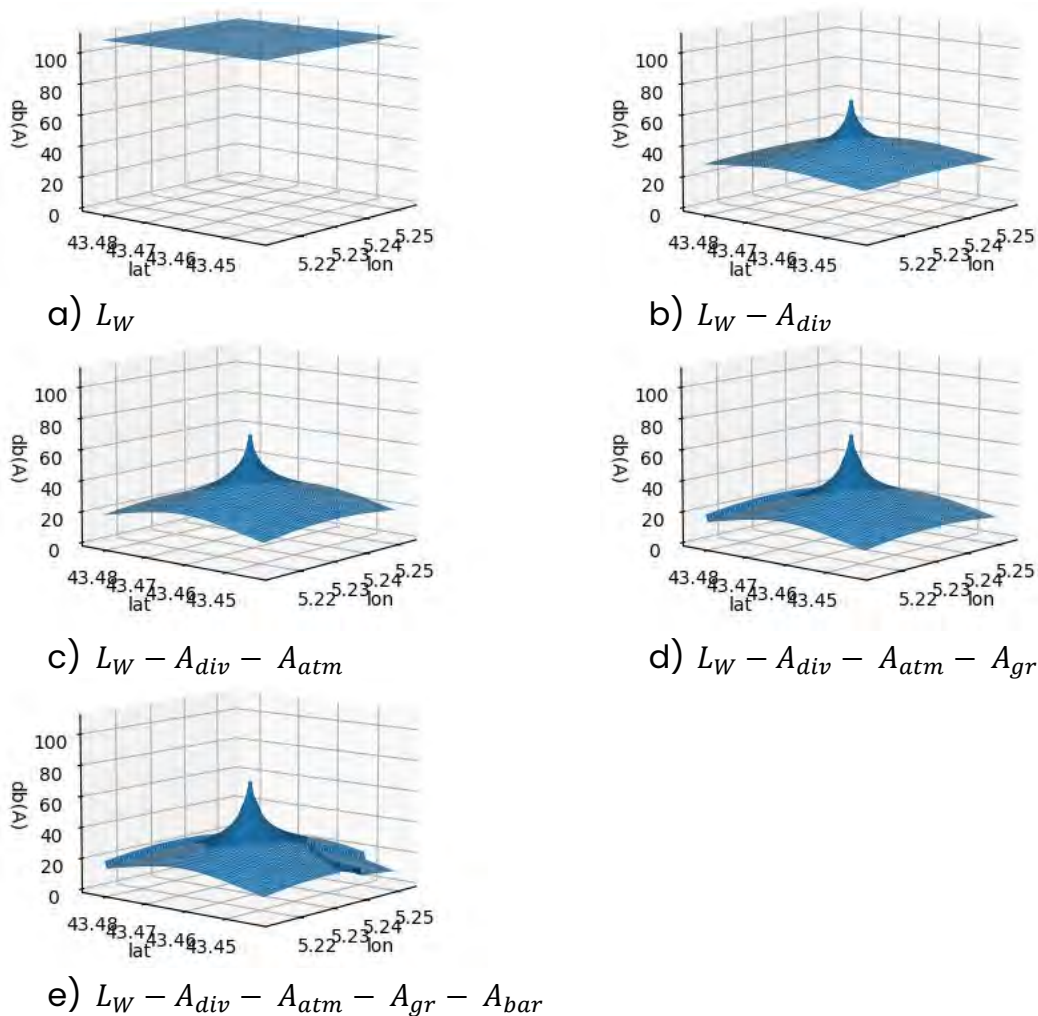


Figure 6 Incremental application of sound attenuation terms on a 2.5 MW wind turbine with a sound power at the source of 108 dB(A), located at 43°27'50.6"N 5°13'52.1"E. L_W : sound power level of the source. A_{div} : sound attenuation due to geometric divergence. A_{atm} : sound attenuation due to atmospheric absorption. A_{gr} : sound attenuation due to ground surface interference. A_{bar} : sound attenuation due to terrain obstacles and barriers.

2.1.5 L_{den}

The L_{den} (Day-Evening-Night Level) metric is a standardised measure to evaluate noise exposure over 24 hours. It incorporates penalties for noise during the evening (+5 dB) and night (+10 dB) to reflect people's increased sensitivity during these times. It is measured in decibels (dB) and is

commonly used for environmental noise assessments, including traffic, industrial, and wind turbine noise.

A very low L_{den} value, typically ≤ 40 dB, is typically found in rural areas, remote countryside, or quiet residential neighborhoods at night. This level is comparable to a whisper or the background noise in a library. At this level, noise is generally not a concern, and there are no significant health impacts.

A moderate L_{den} value, ranging from 40 to 55 dB, can be observed in suburban neighborhoods, parks, or residential areas with some traffic. This level is comparable to the background noise of a quiet office or birds chirping. While it may be noticeable, it is generally considered acceptable for living, with only minor potential for annoyance.

A high L_{den} value, ranging from 55 to 65 dB, is typical for busy urban areas, streets with regular traffic, or homes near railway lines. This level is comparable to the sound of a conversation in a restaurant or background noise in a supermarket. At this level, there is an increased risk of noise annoyance and mild sleep disturbances, particularly during the evening and night.

A very high L_{den} value, ≥ 65 dB, is found near highways, industrial areas, and airports, or close to wind turbines in high-wind conditions. This noise level is similar to that of a loud television or being near a busy road. Prolonged exposure to this level can lead to significant annoyance, sleep disturbances, and potential health effects like hypertension.

In extreme cases, where L_{den} exceeds 75 dB, the noise environment is highly harmful. This can be experienced directly under airport flight paths, near railway crossings with frequent trains, or next to very busy roads with over 50,000 vehicles per day. The noise is comparable to loud music in a club or a vacuum cleaner at close range, and its impact on health is severe, contributing to stress, sleep deprivation, and cardiovascular issues.

The World Health Organization (WHO) recommends an L_{den} below 55 dB for residential areas to minimize health risks. The recommended limit for

nighttime noise is below 40 dB, as excessive noise at night can significantly impact sleep quality.

WindWhisper calculates this indicator for each turbine. The first step involves calculating the wind turbine sound power level ($L_{fT(DW)}$) for each hour of the day processed by DTU based on hourly wind speed data from the bias-corrected ERA5 database (Hersbach et al. 2023). The database generated by DTU provides hourly wind speeds at standard heights (e.g., 10 m, 100 m and 150m), which are linearly interpolated to the turbine's specific hub height. This is an improvement over the previous model version, which relied on the Global Wind Atlas API. The API was too slow, and many requests were returned unfilled.

As stated in D2.3, wind direction is disregarded. Indeed, wind direction shows to have little effect on noise propagation at surface level (0-10m) within a 1'000 m radius from the noise source, as confirmed by the modelling done with WindPRO – Nord2000 module. As cases where listeners would be at a similar elevation as the hub of the wind turbines are uncommon, the effect of wind direction is left out of the modelling scope.

Hence, the final step aggregates the hourly $L_{fT(DW)}$ values into a 24-hour equivalent noise level, incorporating human sensitivity adjustments (i.e., L_{den}).

Hourly $L_{fT(DW)}$ values are converted to linear energy and weighted by period:

- Daytime (07:00–19:00) Energy (E_{day}):

$$E_{day} = 10^{\frac{L_{fT(DW)}}{10}} \cdot 12$$

- Evening (19:00–23:00) Energy ($E_{evening}$):

$$E_{evening} = 10^{\frac{L_{fT(DW)+5}}{10}} \cdot 4$$

- Nighttime (23:00–07:00) Energy (E_{night}):

$$E_{night} = 10^{\frac{L_{fT(DW)+10}}{10}} \cdot 8$$

Note the 5- and 10-dB penalty attributed to Evening and Nighttime noise emissions, respectively.

The total weighted energy over the 24 hours is computed as:

$$E_{total} = \frac{E_{day} + E_{evening} + E_{night}}{24}$$

The final L_{den} value is obtained by converting the total daily energy back to decibels:

$$L_{den(wind)} = 10 \cdot \log_{10} E_{total}$$

2.1.6 Ambient noise sources

A new module in WindWhisper fetches maps of ambient noise sources caused by human activities. The objective is to discriminate the contribution of the wind turbines to the overall sound level for each grid cell.

The module accesses datasets from the European Environment Agency (EEA) Noise Maps², including specific layers for:

- Airports ($L_{airports}$),
- Industry ($L_{industry}$),
- Highways ($L_{highways}$),
- And Railways ($L_{railways}$)

Each dataset is fetched as a GeoTIFF file and processed to assign noise levels in L_{den} using predefined mappings. Missing or null values are replaced with default values (e.g., 0 dB).

² <https://noise.eea.europa.eu/>

The different noise sources are merged into a single dataset. The combination is performed using logarithmic addition:

$$L_{den(amb)} = 10 \cdot \log_{10} \left(\sum_{i=1}^n 10^{\frac{L_i}{10}} \right)$$

Where:

- L_i : Noise level from the i -th source in L_{den} ,
- n : Total number of noise sources.

Then, the ambient noise map ($L_{den(amb)}$) is interpolated to match the spatial resolution and geographic coordinates of the wind turbine noise map ($L_{den(wind)}$), and the total noise level at each grid point ($L_{den(total)}$) is calculated:

$$L_{den(total)} = 10 \cdot \log_{10} \left(10^{\frac{L_{den(amb)}}{10}} + 10^{\frac{L_{den(wind)}}{10}} \right)$$

The net contribution of wind turbine noise to the total noise level ($L_{den(net)}$) is evaluated by isolating the turbine's impact:

$$L_{den(net)} = 10 \cdot \log_{10} \left(\frac{10^{\frac{L_{den(total)}}{10}}}{10^{\frac{L_{den(amb)}}{10}}} \right)$$

Finally, grid points where $L_{den(amb)}$ is below 55 dB(A) but $L_{den(total)}$ exceeds 55 dB(A) are flagged, highlighting regions where the value of 55 dB(A) would be crossed as a result of implementing the wind turbine(s), named L_{impact} . This value corresponds to the EU Commission's threshold for excess exposure defined in the Environmental Noise Directive (The European parliament 2002).

2.1.7 Examples

Figure 7 to Figure 10 illustrate the contribution of a hypothetical 2.5 MW wind turbine to L_{den} noise levels near the village of Sacerno, located close to Bologna Airport. Figure 7 depicts the L_{den} noise emission radii of the wind

turbine in dB(A), indicating that the village of Sacerno experiences noise levels between 30 and 40 dB(A) caused by the turbine operation. In contrast, Figure 8 highlights the impact of existing noise sources (i.e., emissions from Bologna Airport), which subject the village to L_{den} noise levels exceeding 60 dB(A).

Figure 9 presents the overall L_{den} noise levels by integrating the contributions of existing noise sources and that of the hypothetical 2.5 MW wind turbine. Lastly, Figure 10 isolates the net contribution of the wind turbine to L_{den} noise levels. The analysis demonstrates that the wind turbine's contribution is minimal, and it would not increase noise levels experienced by the inhabitants of Sacerno. Consequently, the hypothetical turbine would have a negligible impact on the area's existing L_{den} noise levels.



Figure 7 L_{den} noise emissions of a hypothetical 2.5 MW wind turbine $L_{den}(wind)$, in dB(A), near the village of Sacerno, northeast of the Bologna Airport. Background map: OpenStreetMap.



Figure 8 Existing L_{den} noise emissions $L_{den(amb)}$, in dB(A), in Sacerno, northeast of Bologna Airport, identified using European Noise maps data. Background map: OpenStreetMap.



Figure 9 Overall L_{den} noise emissions $L_{den(total)}$, in dB(A), in Sacerno, northeast of Bologna Airport, considering existing noise sources from the Bologna airport, as well as those from the hypothetical wind turbine. Background map: OpenStreetMap.





Figure 10 Net contribution to L_{den} noise emission levels $L_{den(net)}$, in dB(A), of a hypothetical 2.5 MW wind turbine in Sacerno, northeast of Bologna Airport. Only a limited area northeast of Sacerno sees its exposure to noise levels increase by 30 to 39 dB(A). Background map: OpenStreetMap.

Figure 11 illustrates the attenuating effect of obstacles. In this case, the Sainte-Victoire mountain top separates the village of Puyloubier in France from a 5 MW wind turbine. Downhill noise emissions are attenuated to some extent, preventing the northern district of the Puyloubier village from exposure to noise levels of 30 dB(A) and above.



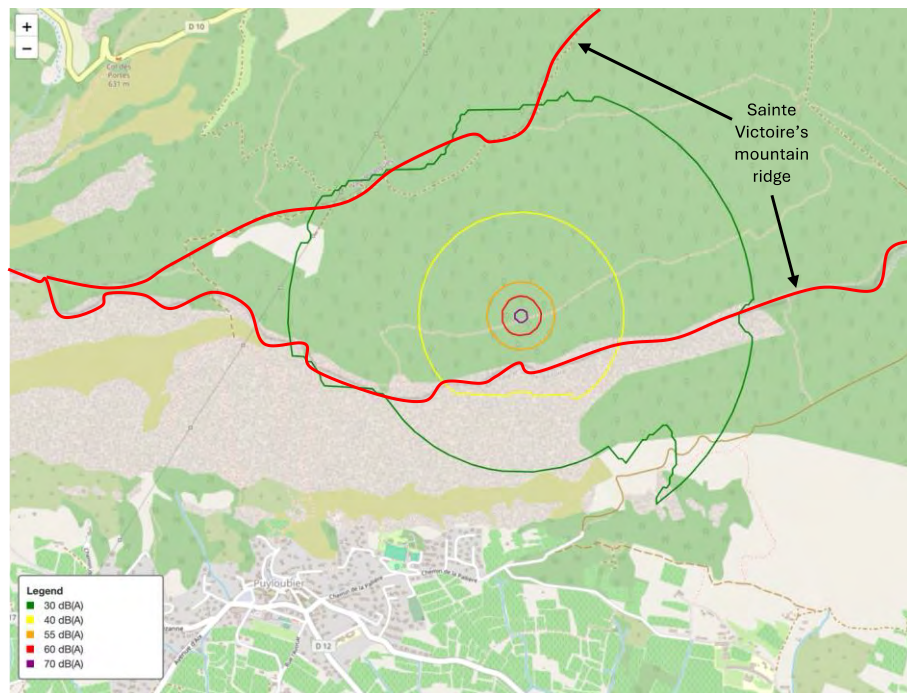


Figure 11 L_{den} noise emission levels of a hypothetical 5 MW wind turbine $L_{den(wind)}$, located at 43°32'14.4"N 5°41'19.9"E, between two ridges of the Sainte-Victoire mountain, overlooking the village of Puyloubier, France. Background map: OpenStreetMap.

2.1.8 Human settlements

After calculating $L_{den(wind)}$ and $L_{den(total)}$, WindWhisper can overlay a layer from the World Settlement Footprint database for the corresponding grid area. This allows the overlay of existing settlements for grid cells, which may be exposed to noise values surpassing the EU's recommended value of 55 dB(A). Using the average dwelling occupation value for the studied area, it is possible to estimate the number of persons exposed to excess noise due to the implementation of wind turbine(s).

2.2 EU maps of potential noise impacts

The result of the workflow described in the previous sections is a multi-layered raster dataset with the following layers: $L_{den(wind)}$, $L_{den(amb)}$, $L_{den(total)}$, $L_{den(net)}$ and L_{impact} . The WIMBY interactive map can readily display such datasets based on users' actions at a specific location.

For D2.4, we provide the HTML static map *Lden_map_Europe_2024-02-28.html* v.1.0.0 that illustrates currently operating wind turbines (i.e., ~90'000 wind turbines, grouped into ~10'000 clusters) in Europe and their net contribution to overall noise levels ($L_{den(net)}$), considering existing noise sources and the difference attenuation terms described above (see Figure 12).

The location, hub height and nominal power are provided for each wind turbine. These parameters are sufficient for WindWhisper to estimate the noise propagation and net contribution. The database listing operating turbines is released under a CC-BY license and is developed by DTU Wind as part of the WIMBY project. It provides harmonised wind turbine position data across Europe, focusing on onshore turbines. Version 2.0.0a (June 2024) of the database combines information from national datasets, OpenStreetMap, the European Marine Observation and Data Network (EMODnet), and other sources, ensuring a comprehensive and harmonised representation of current wind energy infrastructure.

Figure 13 presents a close-up view of Sakskøbing, Denmark, illustrating the contribution of wind turbines to L_{den} levels. The reader will observe the lack of contribution near the city area of Sakskøbing and along the E47 highway.

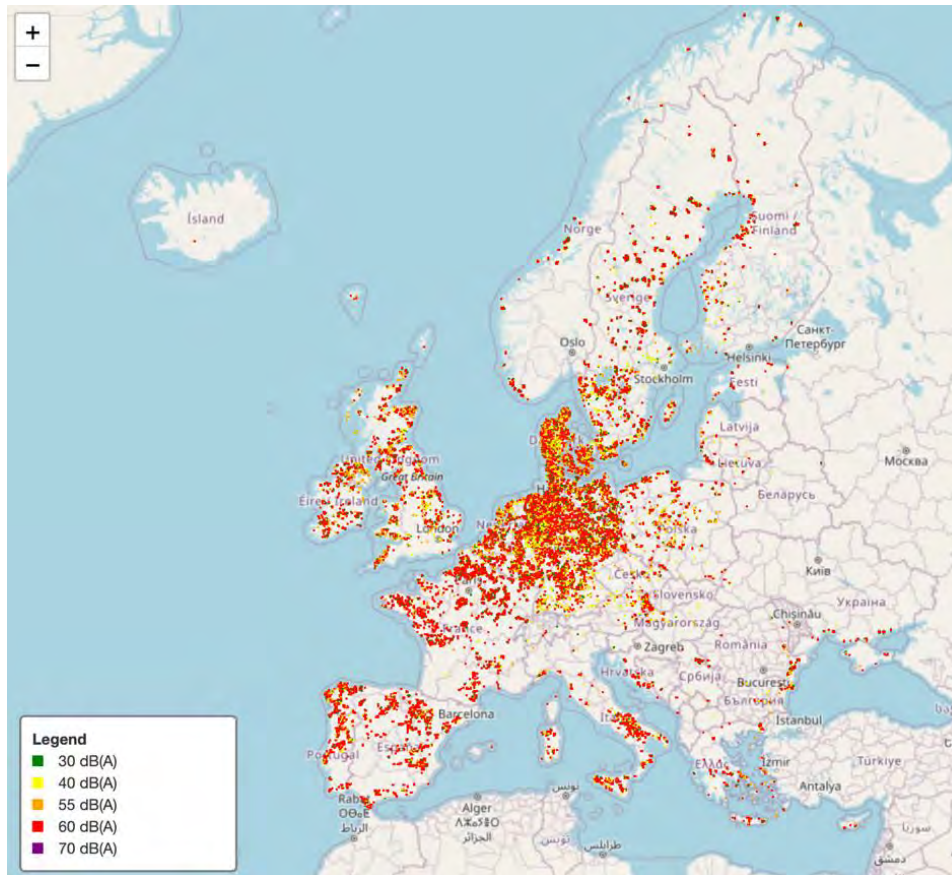


Figure 12 Screen capture of the map showing characterisation of net L_{den} contribution of currently operating wind turbines in Europe. The EU Commission sets the recommended maximum noise level exposure at $L_{den} = 55 \text{ dB(A)}$.

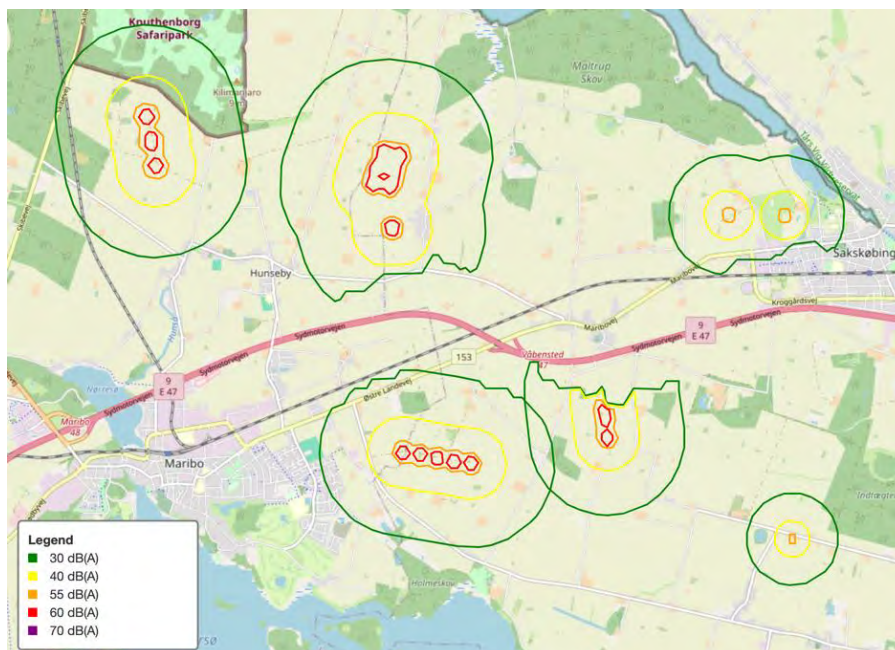


Figure 13 Close-up view on Saksøbing, Denmark, shows wind turbines' net L_{den} contribution.



2.3 Validation

L_W is provided by WindWhisper for a given nominal rated power, hub height and rotor diameter, based on the training on a large dataset of noise measurements (~1470 wind turbines with measurements ranging from 3m/s to 12 m/s), provided by the EMD’s Nord2000 model³.

The multi-output regression model uses a histogram-based gradient boosting algorithm to predict wind turbine noise levels at various wind speeds based on turbine specifications such as power, rotor diameter, and hub height. For licensing reasons, the trained model is made available as part of the WindWhisper package but not the training dataset.

After cleaning, the dataset contains 417 data points, of which 80% are used to train a predictive model. The Root Mean Squared Error (RMSE) in dB (A), obtained after trying to predict noise emissions on the remaining 20% of the dataset, is described in Table 1. Hence, the model has an RMSE of 1.9-1.5 db(A) for low wind speed levels (3-5 m/s), which improves to <1 db(A) for higher wind speeds (≥ 6 m/s).

Table 1 Root Mean Squared Error of noise level prediction, in db(A). Number of data points for training = 333. Number of data points for testing: 84.

	3 m/s	4 m/s	5 m/s	6 m/s	7 m/s	8 m/s	9 m/s	10 m/s	11 m/s	12 m/s
RMSE [db(A)]	1.88	1.26	1.62	1.15	1.06	1.01	0.99	0.99	0.97	0.98

The determination of attenuation terms A and $L_{den(wind)}$, $L_{den(amb)}$, $L_{den(total)}$, $L_{den(net)}$ and L_{impact} is solely based on ISO 9613-2:2024, and shows valid results when considering the presence of natural barriers and existing noise sources.

³ <https://www.emd-international.com/windpro/windpro-modules/environment-modules/nord2000/>

2.4 Calculation time

Table 2 presents the CPU time consumed per wind turbine simulation. Due to vectorized array operations, the CPU time required for each simulated turbine decreases as the number of turbines increases. However, note that the wall time (i.e., the time spent waiting for API responses) can significantly raise the total process time.

Table 2 CPU time for computing L_{den} noise contours for various wind turbines. CPU time (WindWhisper) = CPU time spent executing code that belongs to the WindWhisper model. CPU time (system) = CPU time spent executing code outside the WindWhisper model.

Number of wind turbines	CPU time (WindWhisper) [second]	CPU time (system) [second]	CPU time (total) [second]	CPU time (total) per turbine [second]
1	1.4	0.914	2.31	2.310
10	1.4	0.472	1.83	0.182
100	4.9	1.21	6.09	0.061
1000	33.6	4.52	38.1	0.038

3. Shadow flicker tool

3.1 Tool improvement from version a

Numerous improvements have been made to the first version (version A) of the shadow flicker tool (SF tool) described in D2.3. First, wind conditions have been integrated, allowing users to consider wind speed data and provide an SF assessment closer to operational conditions. Second, the calculation of shadow geometry has been refined to account for the sun's angular diameter and the growth of the shadow's penumbra. Third, in the new version, the model considers the topography. We adapted the shadow flicker calculation to align with topography data obtained from a digital elevation model.

3.1.1 Including wind condition in shadow flicker tool

Wind turbines have specific cut-in and cut-out wind speeds; therefore, the model must consider wind speed data. The more instances throughout the year that the wind speed is below the cut-in or above the cut-out speed, the less shadow flicker occurs because the turbine remains stationary. The initial version of the SF_tool assumed that the turbine was continuously rotating, representing the worst-case scenario for shadow flicker calculations.

We have added a flag, `consider_wind_conditions = True (or False)`, to allow the user to choose between the worst-case scenario calculation and one that more accurately reflects operational conditions. When the condition, `consider_wind_conditions`, is True, a new script, `shadow_flicker_wind`, will be executed. This prevents the calculation of time steps with wind speeds lower than the cut-in speed and higher than the cut-out speed.

We use the ERA5 mean wind speed 12 x 24 dataset along with associated data derived from the Global Wind Atlas for bias correction generated by DTU, provided in netCDF format (Hersbach et al. 2023). The 12 x 24 dataset was created by averaging data from the time period 2013–2022 for an area covering Europe, specifically from 35N to 72N and 15W to 35E, with a horizontal grid spacing of 0.25 degrees by 0.25 degrees (Hersbach et al. 2023). The bias correction is applied to obtain higher spatial resolution data, including average wind speeds at three heights (50, 100, and 200 m) over the course of the month and hour of the day.



By default, the cut-in speed is set at 3 m/s, while the cut-out speed is 25 m/s. Users have the option to customize these speed preferences. For integration in the WIMBY interactive map, these values will be taken from the turbine model description. At each time step and turbine location, the model retrieves the hourly mean wind speed from the bias-corrected 24x12 dataset. If the wind speed exceeds the cut-out speed or falls below the cut-in speed, we assume that the wind turbine is not operating and, therefore, is not generating shadow flicker.

3.1.2 Improving the shadow geometry calculation

This improvement includes three sub-steps: a) shadow shape correction by including shadow umbra and penumbra and b) shadow geometry angle and location.

In the first version of the SF tool, the shadow polygon was transformed from the turbine rotor only based on the sun angles. By using trigonometric projection, the shadow length L is given by:

$$L = h \cdot \tan(90^\circ - \varepsilon_s)$$

Where:

$$h = \textit{Turbine height}$$

$$\varepsilon_s = \textit{Solar elevation(degrees above horizon)}$$

And if $L > L_{max}$ no shadow is computed since it exceeds the maximum shadow distance. The shadow is located in the direction opposite to the sun azimuth, shifted from the turbine location with shadow length, with the turbine rotor polygon as geometry.

Shadow direction:

$$\theta = \alpha_s + 180^\circ$$

Shadow position:

$$(x', y') = (x - L\cos\theta, y - L\sin\theta)$$

Where:

$$\alpha_s = \textit{Solar azimuth}$$



$(x, y) = \text{Turbine location}$

However, the shadow of the turbine rotor should appear as an ellipse and be extended according to the sun's angle, meaning it becomes longer when the sun's elevation is nearer to the horizon. We developed the shadow-transforming method for the turbine rotor as detailed below.

A) Shadow umbra and penumbra

When an object (e.g., a wind turbine rotor) blocks sunlight, the total shadow formed behind it can be divided into two regions (Salazar Trujillo 2014):

1. **Umbra:** The region of full shadow, where the light source is entirely blocked.
2. **Penumbra:** A partially shadowed area where only part of the light source is obscured. Since the Sun is not a point source as seen from Earth but rather has an apparent disk with a diameter of about 0.53° , there exists a "fuzzy" boundary region around the umbra known as the penumbra (Figure 14).

Therefore, when considering both the umbra and penumbra regions, the rotor's shadow is **wider** than the physical size of the rotor because the sun is not a perfect point source. This widening happens because various parts of the sun's disk are obscured at slightly different angles.

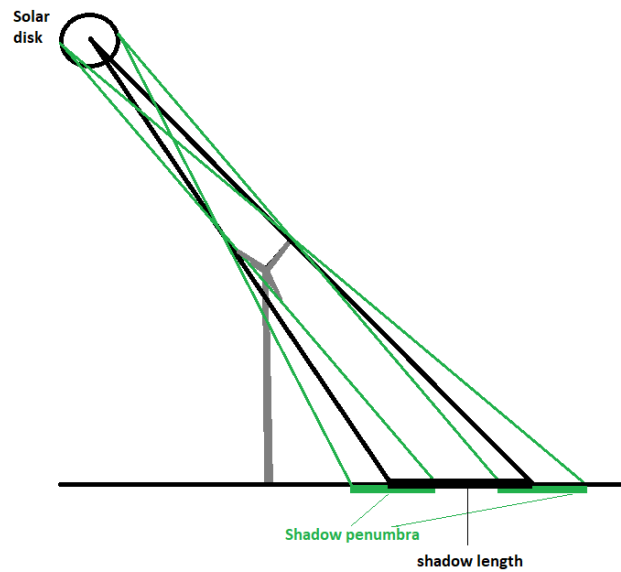


Figure 14 Illustration of the shadow penumbra at the edge of a wind turbine's full shadow.

An approximation to penumbra width can be calculated by the sun's angular diameter $\alpha \approx 0.53^\circ$. The penumbra width in Figure 14, denoted by W_p is:

$$W_p = D + 2L \tan(\alpha_{rad})$$

Where:

$$D = \text{Turbine rotor diameter (m)}$$

$$L = \text{The shadow length (m)}$$

$$\alpha_{rad} = \alpha \times \pi / (180^\circ)$$

This indicates the width of the partial shadow region at the distance L behind the turbine – equations are based on (Salazar Trujillo 2014).

If we consider the turbine rotor as a disc during operation, the projected shadow of the turbine rotor should form an elongated ellipse rather than maintaining the original turbine rotor geometry. To transform the circular rotor plate P into an ellipse, we utilize the shadow length L and penumbra width W_p generated above to calculate the major and minor axes S_y of the shadow ellipse:

$$S_x = L/R$$

$$S_y = W/D$$

This scales each point $(x', y') \in P$ to:

$$(x'', y'') = (x' \cdot S_x, y' \cdot S_y)$$

B) shadow geometry angle and location

After transforming the shape, the ellipses need to be rotated to the correct shadow orientation, which aligns with the shadow direction. We use the 2-dimensional rotation matrix here for rotation factor R_θ :

$$R_\theta = \begin{bmatrix} \cos\theta & -\sin\theta \\ \sin\theta & \cos\theta \end{bmatrix}$$

Applying the rotation:

$$\begin{bmatrix} x''' \\ y''' \end{bmatrix} = R_\theta \begin{bmatrix} x'' \\ y'' \end{bmatrix}$$

Finally, translate the ellipse to its correct shadow location:

$$\Delta x = -L \cos\theta, \quad \Delta y = -L \sin\theta$$

$$(x_{final}, y_{final}) = (x''' + \Delta x, y''' + \Delta y)$$

In the end, the resulting shadow footprint is given by:

$$S = \tau_{\Delta x, \Delta y} \left(R_\theta \left(S_{x,y}(P) \right) \right)$$

Where:

$\tau_{\Delta x, \Delta y}$ represents the **translation**;

$S_{x,y}$ applies the **rotation**; and
performs the **scaling**.

The difference in the SF assessment using the final and the first version of the SF tool is shown in Figure 15. The new version enhances the representation of the areas affected by SF. It also covers a larger area at each time step, resulting in increased shadow flicker coverage hours.

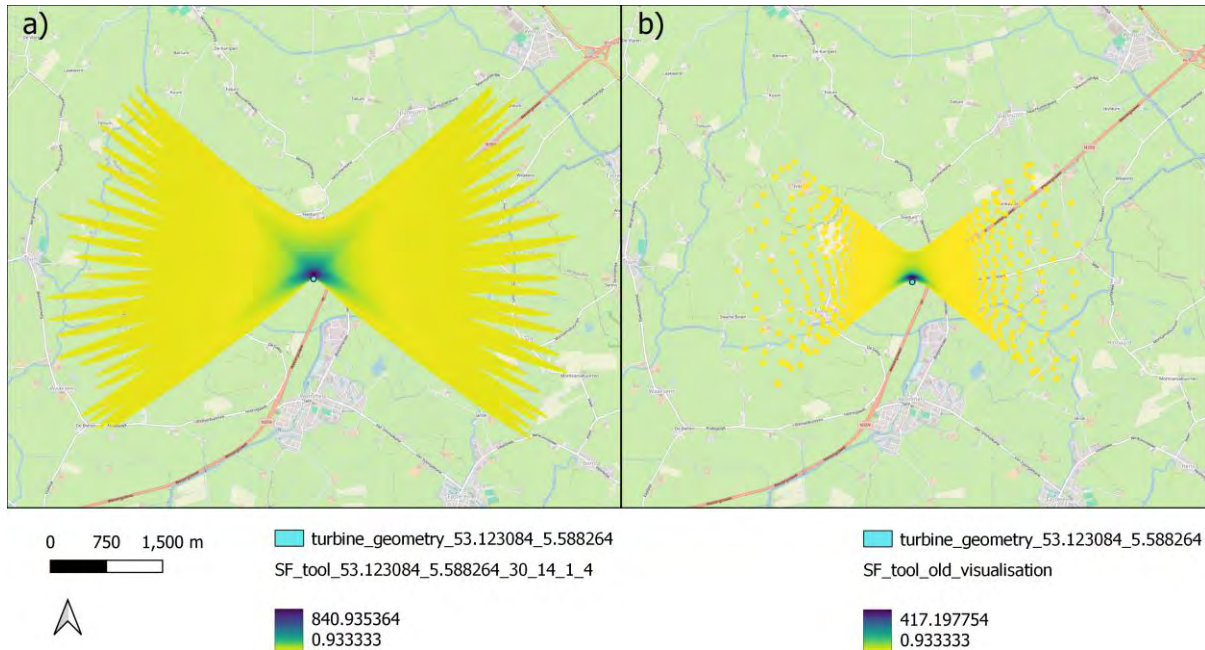


Figure 15 a) The new SF_tool result, with corrected shadow geometry. b) The shadow flicker results from the previous version of SF_tool, taking turbine geometry as shadow geometry.

To validate our modeling results for shadow flicker projection, we used SF_tool and WindPRO for 50 turbine locations in the Netherlands representing (almost) flat terrain cases, and then compared the results from both tools. The 50 turbines were selected at equal distances from the north to the south of the Netherlands, with latitude 5.852967 and a longitude range of 50.78 to 53.38 to encompass the north-south land area as much as possible. Ultimately, only 48 turbines were employed for the statistical analysis because two of the turbine locations were situated in more hilly regions. One of the comparison results is displayed in Figure 16. Overall, both tools cover similar areas, indicating that the improved simulation method is highly aligned with the WindPRO results.

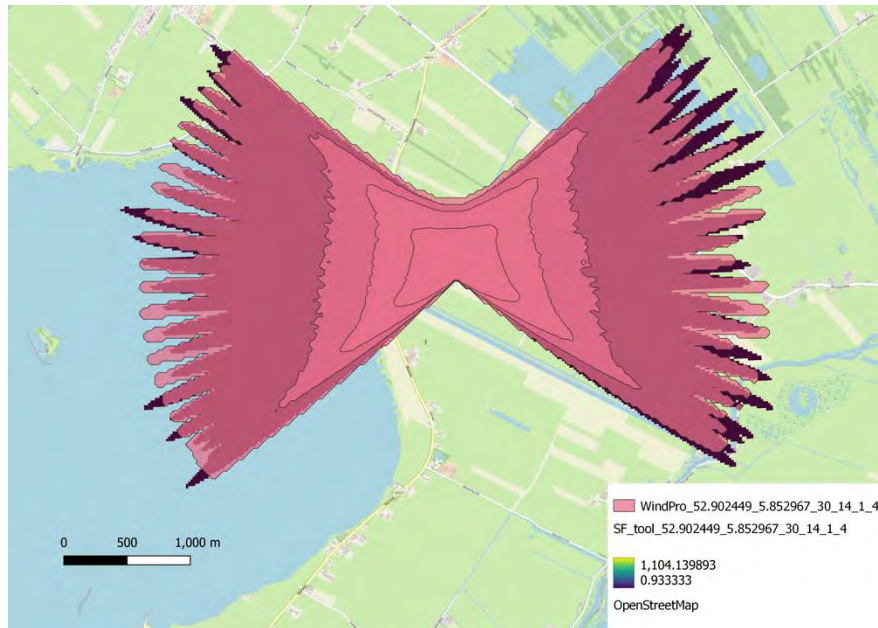


Figure 16 The updated SF tool result in the Netherlands (yellow to dark blue area) compared to the WindPRO result at the same location (52.902449, 5.852967.)

To deliver a quantitative validation, considering that the edges of the SF map could change considerably due to internal algorithm parameters (which we cannot determine from WindPRO), such as the starting time for the solar altitude calculation, we decided to focus the comparison on the area of shadow flicker relevant to the permission processes of wind farms. We rely on the results of the regulations overview provided in D2.10. From the KIE work in that deliverable, we know that in 2002, Germany introduced a guideline for calculating and evaluating shadow flicker based on scientific research (Länderausschuss für Immissionsschutz 2002). This guideline has since established the foundation for shadow flicker regulations and assessment frameworks in many other countries (Koppen, Gunuru, and Chester 2017). The German standard was revised in 2019 (Bund-/Länder-Arbeitsgemeinschaft für Immissionsschutz (LAI) 2020), setting a shadow flicker threshold of **30 hours per year** and **30 minutes per day** under the **astronomical worst-case scenario**—representing the maximum possible shadow duration (Koppen and Ekelschot-Smink 2023). Therefore, we conducted the statistical analysis for areas with more than 30 hours of shadow flicker from the outputs of our SF_tool and WindPRO for validation.

Figures 17 and 18 illustrate the area’s highest and lowest overlap cases with over 30 hours per year of shadow flicker impacts. The lowest overlap occurs due to the rising topography on the northern side as shown in Figure 18, since we have not included the impacts of topography at this stage. The contour lines on the maps represent changes in topography. Figure 17 features only a 50m contour line, indicating a relatively flat and uniform terrain, while Figure 18 includes both 50 m and 100 m contour lines, reflecting a more hilly and varied landscape.

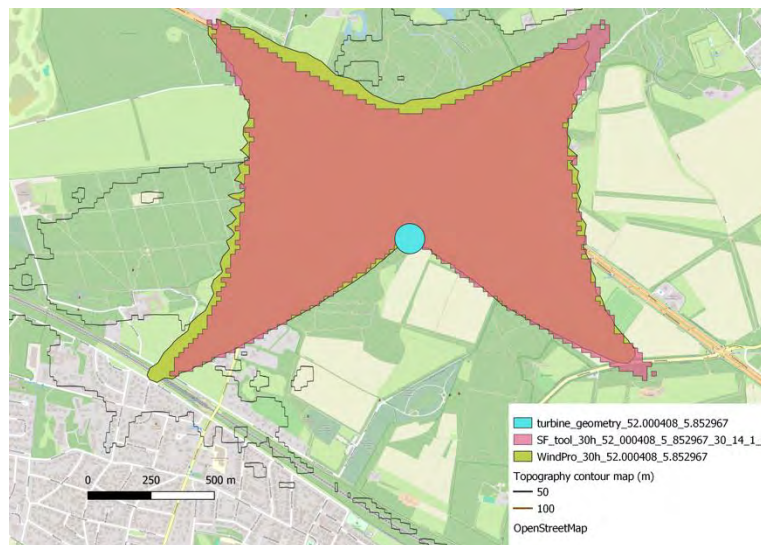


Figure 17 The highest overlapping case. The turbine geometry is shown as a light blue circle at (50.000408, 5.852967). The green area represents the shadow flicker coverage region greater than 30 hours/year simulated by WindPRO; the pink area represents the coverage area greater than 30 hours/year modelled by SF_tool. The topography contour map only contains the contour line up to 50 meters (in black), indicating a relatively flat and homogeneous terrain.

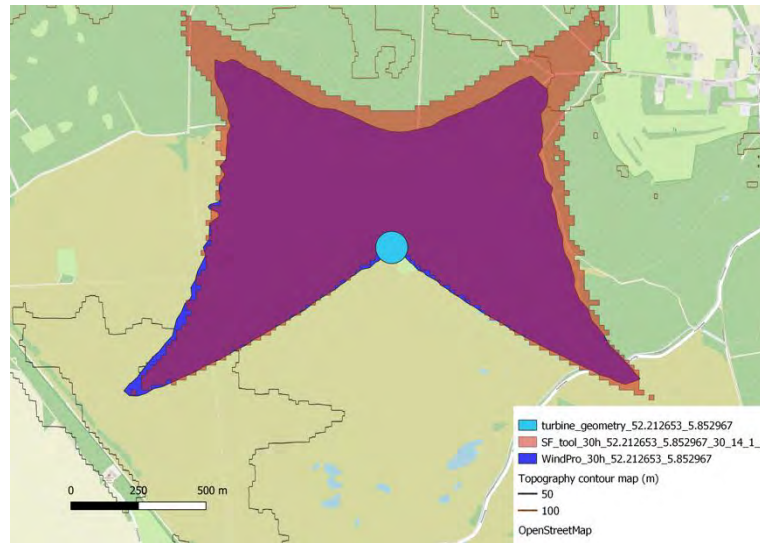


Figure 18 The lowest overlapping case. The turbine geometry is shown as a light blue circle at (52.212653, 5.852967). The darker blue area represents the shadow flicker coverage region greater than 30 hours/year simulated by WindPRO; the orange area represents the coverage area greater than 30 hours/year modelled by SF_tool. The topography contour map shows the 50- and 100-meter lines (in black and brown), indicating more hilly terrain, especially on the map's northern side.

The descriptive statistics for the area >30 hours for 48 turbines show:

- **SF_tool** mean area $\approx 3.35 \times 10^6$ (with std $\approx 1.56 \times 10^5$) m².
- **WindPRO** mean area $\approx 3.18 \times 10^6$ (with std $\approx 2.13 \times 10^5$) m².

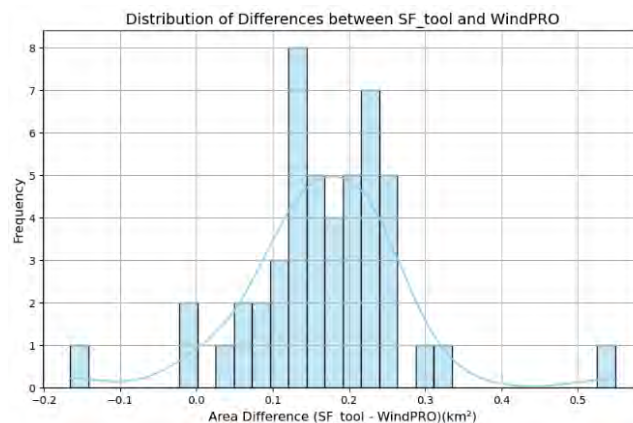


Figure 19 Distribution of differences between SF_tool and WindPRO simulation for the area with >30hr/year shadow flicker impact in the Netherlands validation.

These summary statistics suggest that, on average, the SF_tool areas are slightly larger than those from WindPRO. We also conduct a correlation analysis using Pearson's correlation, which is approximately 0.889. This indicates a strong positive relationship between the two sets of area

simulations (Figure 20a). Therefore, the SF_tool performs well under flat topography conditions. Figure 19 also shows a roughly bell-shaped distribution, suggesting that most differences hover around the mean, with a few outliers on either side.

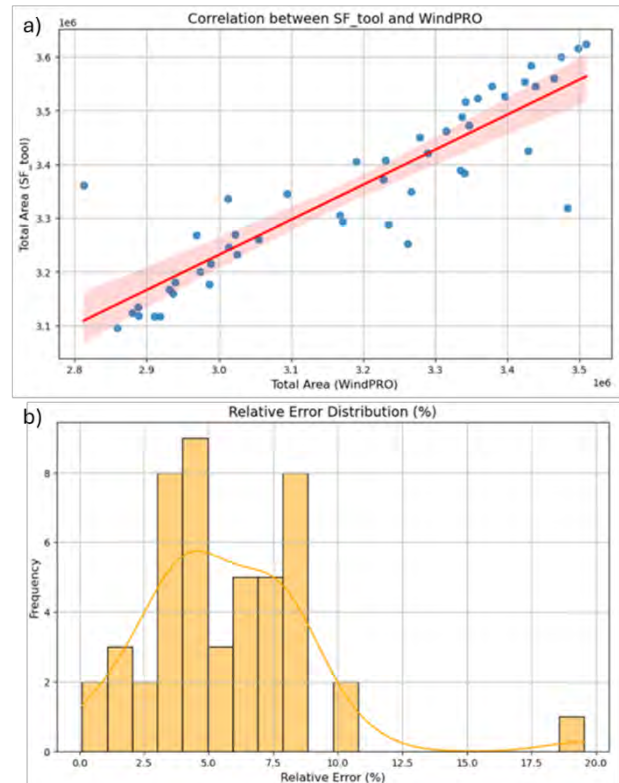


Figure 20 a) Correlation between SF_tool and WindPRO for the validation in the Netherlands. This figure shows SF_tool > 30hr/year areas (y-axis), the WindPRO > 30hr/year areas (x-axis), and the regression line. b) Relative error distribution histogram between the shadow flicker simulation results (> 30hr/year area) of SF_tool and WindPRO.

The relative error distribution histogram (Figure 20 b) highlights the percentage error between SF_tool and WindPRO. It indicates that typical discrepancies remain within a reasonable range (often less than 10%). A peaking error distribution at a low value suggests that most estimates are relatively close. The range and peak of relative errors are between 2–8%, with an outlier exhibiting a relative error of around 18% (the lowest overlap case in Figure 20 b)), which can be attributed to topography.

In conclusion, the SF_tool performs well in flat terrain if we take WindPRO simulation results as a reference. The strong correlation (≈ 0.889) implies that both tools vary in tandem, suggesting that while SF_tool might systematically report higher areas, it remains consistent with WindPRO's relative differences across different turbine locations.

3.1.3 Shadow flicker accounting for topography

To include topography impacts in shadow flicker calculation, we should consider two key facts:

- a) The shadow geometry transforms when projecting on hilly areas.
- b) If the spot is already in the topography shade (e.g. behind a hill), then there is no shadow flicker impact on the spot.

Most literature mainly focuses on part b), therefore developing the visibility algorithm, but rarely discusses the shadow transformation on terrain. Hence, for part a), we developed a new method to calculate the potential shadowed area for a turbine in non-flat terrain, using a digital surface model (DSM) as input. To maintain input data consistency with other tools in the WIMBY interactive map, we utilize the Copernicus DSM (30m) (European Union 2022). To address part b), we calculate a viewshed using the GDAL viewshed tool, and then create a mask for the viewshed area of the target turbine.

3.1.4 Shadow geometry transformation on topography

To calculate the potential shadowed area for a turbine, we first retrieve the turbine elevation from the DSM. Then, based on the elevation height and turbine rotor diameter, three maps are generated: the altitude angle map toward the top of the turbine rotor (α_{top}), the altitude angle map toward the bottom of the turbine rotor (α_{bot}), and the azimuth angle map toward the turbine (β), as outlined in Nagy (1994).

For each pixel (i, j) in the DSM:

$$\Delta x = x_{WT} - x_{ij}, \Delta y = y_{WT} - y_{ij}$$



Horizontal distance:

$$dist = \sqrt{\Delta x^2 + \Delta y^2}$$

Altitude angle (α):

$$\alpha_{ij} = \arctan 2 (\Delta z, dist)$$

Azimuth angle (β):

$$\beta_{ij} = \arctan 2 (\Delta x, \Delta y)$$

We generate two maps α_{top} and α_{bot} with the degrees "looking up (or down)" toward turbine rotor top and turbine rotor bottom (Figure 21(a) and 21(b)), and one map β that shows the "horizontal angle" from the south toward the turbine for each pixel (Figure 21 (c)).

For sun altitude and azimuth, the angles are calculated based on time step t . The data row for time t contains:

- Solar altitude (rotor top): $A_{top}(t)$
- Solar altitude (rotor bottom): $A_{bot}(t)$
- Solar azimuth: $B(t)$

Considering the sun's angular diameter ($\sim 0.53^\circ$),

$$A_{top_min}(t) = A_{top}(t) - \frac{0.53}{2}$$

$$A_{bot_max}(t) = A_{bot}(t) + \frac{0.53}{2}$$

Then we create a mask M_{alt} where each pixel must satisfy:

$$\alpha_{top} \geq A_{top_min}(t), \alpha_{bot} \leq A_{bot_max}(t)$$

$$\text{i.e., } M_{alt} = \left(\alpha_{top} \geq A_{top_min}(t) \right) \wedge \left(\alpha_{bot} \leq A_{bot_max}(t) \right)$$

The intermediate maps in Figure 21 (d) and (e) represent map $\left(\alpha_{top} \geq A_{top_min}(t) \right)$ and map $\left(\alpha_{bot} \leq A_{bot_max}(t) \right)$. Figure 22 (a) shows M_{alt} . In short, to

calculate the potential shadow area of the turbine rotor, we look for the different areas between Figure 21 (d) and 21(e), then get the "doughnut" map of Figure 22(a).

Next, we compare each pixel's (turbine) azimuth angle β_{ij} with sun azimuth $B(t)$ under tolerance angle τ . Then define an azimuth mask:

$$M_{az}(i, j) = \begin{cases} 1, & \text{if } |(B(i, j) - B(t) + 360) \% 360| \leq \tau, \\ 0, & \text{otherwise.} \end{cases}$$

In this step, we find the range when the turbine azimuth angle is aligned with the sun azimuth angle (Figure 22 (b), taking a tolerance angle = 5° as a buffer here for illustration).

Finally, combining the altitude mask M_{alt} and azimuth mask M_{az} , the shadow map M_{shadow} can be defined as below:

$$M_{shadow}(i, j) = M_{alt}(i, j) \wedge M_{az}(i, j)$$

Therefore, by overlapping the azimuth mask with the potential "doughnut" shadow map (the altitude mask), we obtain the shadow area cast by the turbine rotor at that specific time step (t) in Figure 22 (c), which can be viewed as the shadow footprint (t).

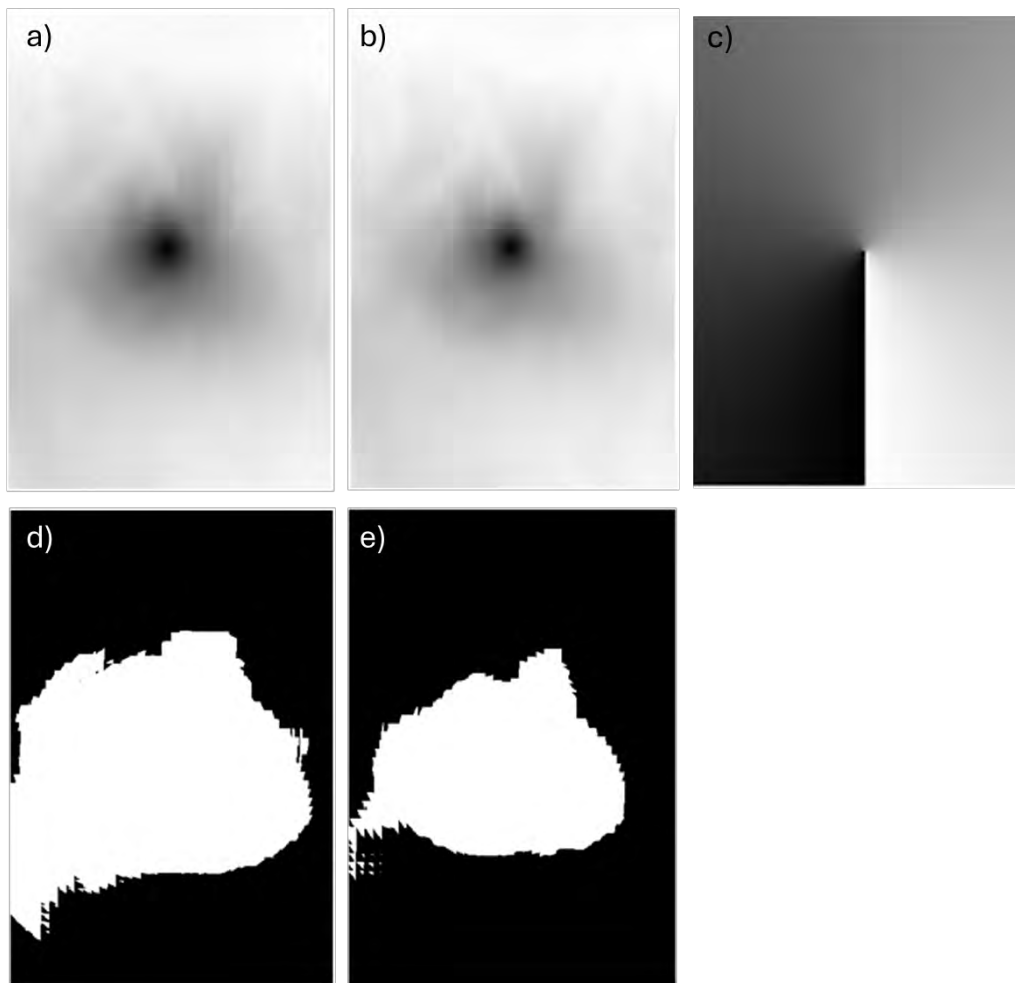


Figure 21 (a) and (b) represent the altitude maps, showing the vertical angles from each pixel to the turbine rotor top and bottom, respectively. (c) represents the azimuth map, which indicates the direction of each pixel relative to the turbine. (d) highlights the pixels that can be cast into shadow from the turbine rotor top, while (e) represents those cast from the turbine rotor bottom.

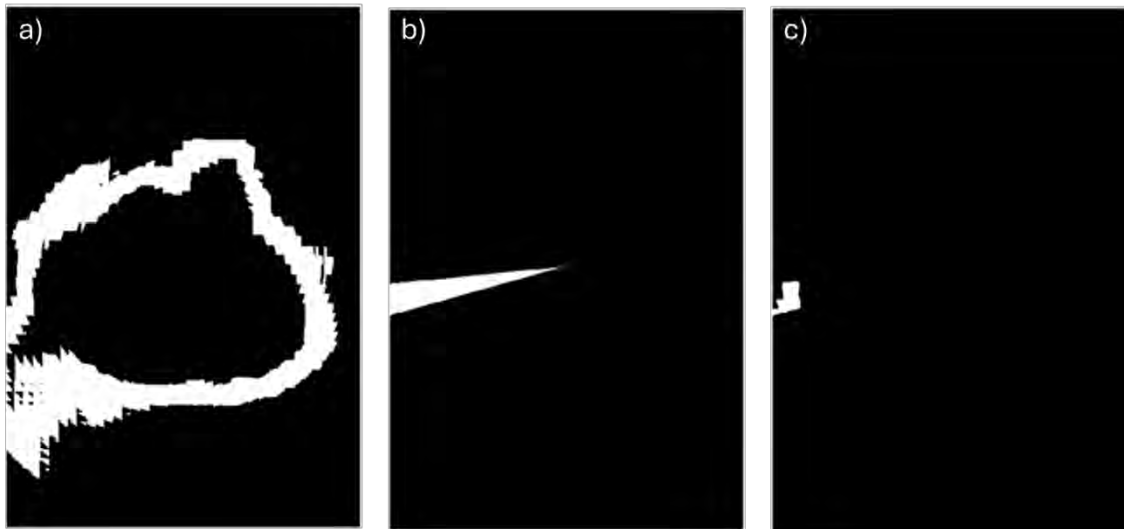


Figure 22 (a) depicts the altitude mask, computed as the difference between the altitude maps for the turbine rotor top and bottom. This highlights the potential shadow-casting area. (b) illustrates the azimuth mask, incorporating a tolerance of 5°. (c) presents the overlapping region of (a) and (b), effectively delineating the final shadow footprint at a given time step.

However, at this step, the shadow area is still missing the ellipse shadow geometry we discussed in section 3.1.2. Therefore, we take the location and the maximum length (parallel to the sun's azimuth) of this area as the shadow length and shadow location, and apply the algorithm from section 3.1.2 to calculate the shadow flicker footprint.

Consequently, we obtain the shadow flicker map that takes into account the terrain transformation shadow projection (Figure 23).

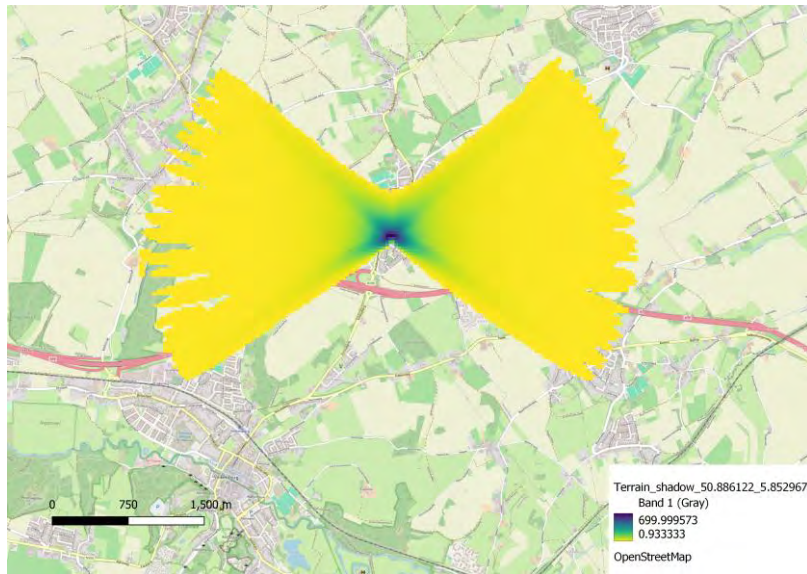


Figure 23 The shadow flicker map includes shadow transformation on terrains, with turbine location (50.866422, 5.852967) in the Netherlands.

B) Viewshed application

In the final step, we create a visibility map to identify topographical obstructions. This map uses the turbine's location and elevation height (of the center of the turbine rotor) as the "observer" location and calculates the viewshed map from the turbine. Consequently, the viewshed area in this map has obstacles between the turbine and cannot be "seen" from the turbine, meaning the turbine's shadow cannot cover it either. The goal is to generate this map and exclude the viewshed area from the transformed shadow flicker map above (Figure 23).

We use `gdal_viewshed`, which can be applied to a given DSM and a chosen location, by instructing GDAL to compute line-of-sight from observer at (X_0, Y_0, h_0) and max distance M (10 km here). Where X_0, Y_0 is the turbine location and $h_0 = \text{turbine height} + \text{elevation}$ in our calculation.

Mathematically, each pixel (X, Y) is visible from the observer if there is no point on the line segment between (X_0, Y_0) and (X, Y) where the DSM surface height exceed the line-of-sight.

Hence, if at any sampled point (X_i, Y_i) ,

$$\text{surface Height}(X_i, Y_i) > h_0 - (h_0 - \text{surface Height}(X, Y)) \times \frac{\text{dis tan ce}(X_0, Y_0, X_i, Y_i)}{\text{dis tan ce}(X_0, Y_0, X, Y)}$$

the line of sight is blocked, and the pixel (X, Y) is **not visible**.

In addition, we use a bounding box of size $\pm 5 \text{ km}$ from the turbine center to clip the DSM and calculate the viewshed for each turbine.

Here, we present the example using `gdal_viewshed` for the same turbine in Figure 23 and then exclude the viewshed area to get the final shadow flicker map (Figure 24). As shown in Figure 24, the viewshed area is marked as black; after filtering out these areas, we get the final shadow flicker map, taking terrain factors into account.

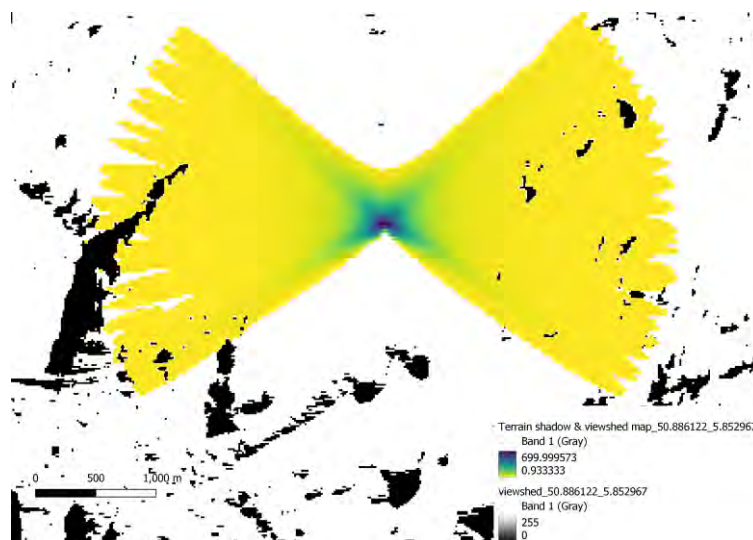


Figure 24 Shadow flicker map excluding the viewshed area (in black), for turbine location (50.866122, 5.852967) in the Netherlands.

Figure 25 illustrates the distribution of shadow flicker in a mountainous region of Spain, overlaid on the EU DSM resampled to 20 m. Resampling to 20 m, instead of using the original 30 m DSM, was necessary to maintain the accuracy of the angle maps (α_{top} and α_{bot}). A coarser resolution can lead to distorted and imprecise angle calculations, especially when the sun's altitude approaches 90° around midday, affecting the projection of shadow flicker. The analysis shows that SF_tool effectively captures the influence of topography, incorporating elevation variations into the viewshed and projection of shadow flicker. The shadow flicker area (dark regions) corresponds with terrain features, demonstrating how elevated landforms obstruct or extend shadow propagation. This visualization confirms that SF_tool effectively integrates topographic factors, enhancing its predictive reliability in complex landscapes.

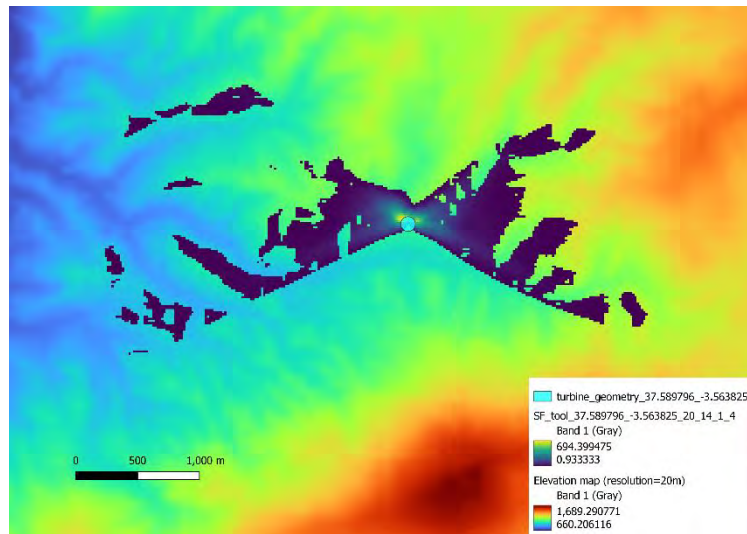


Figure 25 Shadow flicker distribution in a mountainous region of Spain. The shadow flicker map (dark regions) is overlaid on an elevation map, demonstrating the influence of topography on shadow propagation. Higher elevations (red-orange) and lower areas (blue-green) affect the extent and shape of flicker exposure.

To validate the results while considering topographic influence, 50 turbine locations across Spain were selected, covering the longest land extent from north to south and intersecting mountainous regions (latitude: 36.9–39.5, longitude: -3.563825).

For statistical analysis, regions experiencing over 30 hours per year of shadow flicker were selected to compare the results between SF_tool (which accounts for topography) and WindPRO. Descriptive statistics indicate that SF_tool estimates a mean shadow flicker area of 808,686 m², while WindPRO reports a mean of 811,090 m². Although SF_tool's estimations are slightly lower, the difference is negligible (approximately 0.3%). Additionally, SF_tool exhibits a higher standard deviation, suggesting greater variability in its estimations (Table 3).

Table 3 The descriptive statistics of Spain cases between SF_tool and WindPRO, considering the topography impacts in SF_tool.

Metric	SF_tool	WindPRO
Mean Total Area (m ²)	808,686	811,090
Standard Deviation	161,780	111,439
Minimum	469,129	547,117
Maximum	1,138,393	1,044,514

The Pearson Correlation is 0.907 in Figure 26, which suggests a strong positive correlation, meaning both tools exhibit a consistent trend across different locations. The red regression line with a narrow confidence interval suggests high consistency. Outliers at higher total areas indicate locations where SF_tool diverges slightly from WindPRO. The p-value is 0.932 (>0.05), which indicates no statistically significant difference between the two tools.

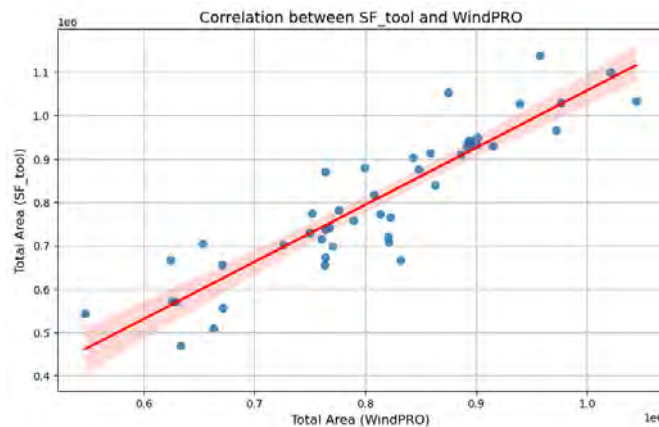


Figure 26 Correlation Between SF_tool and WindPRO for validation in Spain cases.

Figure 27 illustrates the distribution of absolute differences between SF_tool and WindPRO. The majority of these differences cluster around zero, indicating a strong overall agreement between the two tools. However, a few extreme values, both positive and negative, suggest localized variations in specific areas. These discrepancies are more pronounced in regions where the terrain surrounding the turbine—defined as areas experiencing more than 30 hours of shadow flicker per year—is highly fragmented or exhibits significant elevation changes. The observed variations can be attributed to two primary factors: (1) SF_tool employs a higher-resolution viewshed analysis (20m), capturing finer terrain details, and (2) differences in the

computational methods used by SF_tool and WindPRO to model shadow transformation on hilly terrain; for instance, it appears that WindPRO may not implement the same terrain shadow transformation as SF_tool (Section 3.1.3(A)). Since WindPRO’s shadow flicker algorithm is proprietary and therefore not fully transparent, we can only infer these differences from the observed outcomes.

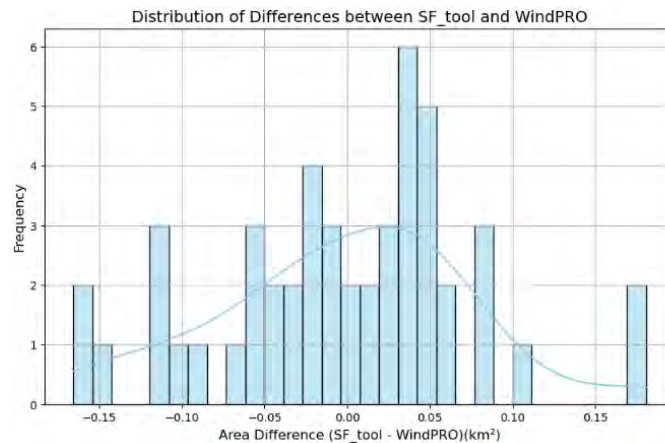


Figure 27 Distribution of differences between SF_tool and WindPRO for validation in Spain cases.

The relative error distribution depicted in Figure 28 illustrates the percentage of relative error between the two models. Most errors are below 10%, suggesting that SF_tool offers reliable estimations. A few cases exceed a 15% error, which may be attributed to the influences of complex terrain.

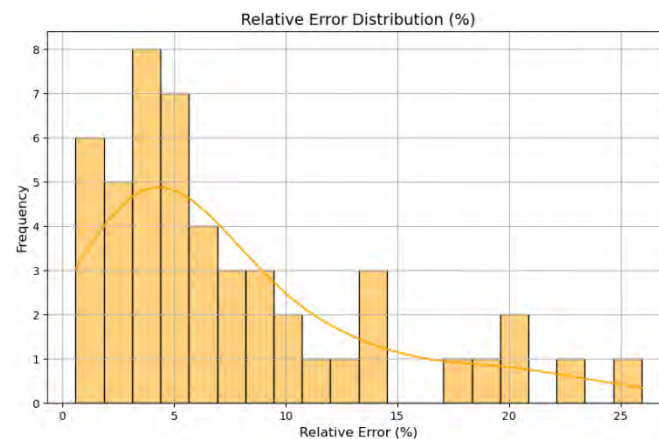


Figure 28 Relative Error Distribution for validation in Spain cases.

3.1.5 Visualization



Figure 29 presents a final shadow flicker map depicting terrain impacts. However, the figure's presentation fails to highlight the differences in shadow flicker coverage frequency, which does not facilitate effective communication.

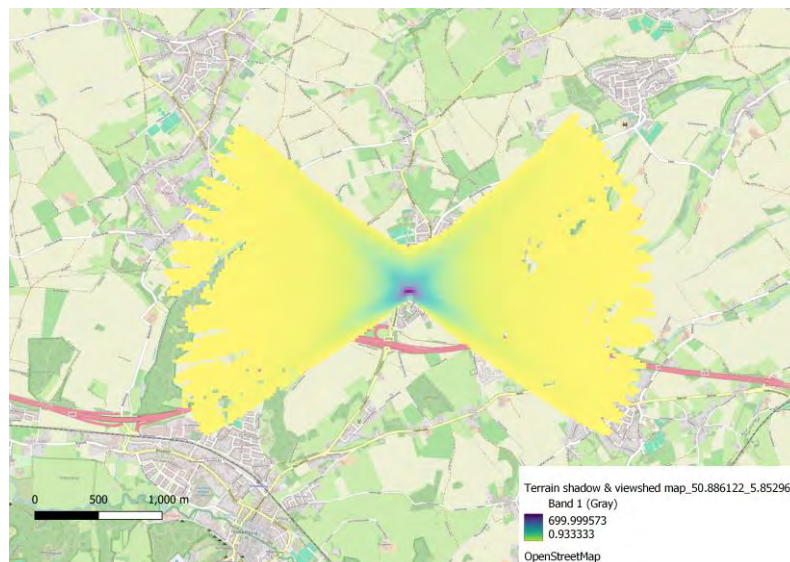


Figure 29 A final shadow flicker map in the Netherlands. The final shadow flicker map incorporating viewshed analysis and transformed shadow propagation, with shadow flicker frequency represented using a gradient colour scale.

Since we aim to integrate this tool into the WIMBY interactive map, we discussed with the WIMBY consortium how to optimize the visualization of our shadow flicker map. The first idea was a contour map showing shadow coverage hours of 10, 30, and 100 (Figure 30). During the discussion, two issues with this figure were pointed out. Firstly, although this time interval is easier to understand, it is challenging to relate it to the number of hours over a year. Additionally, the contour details do not provide more useful information than simply showing the contour for 30 hours and the area of >0 hours.

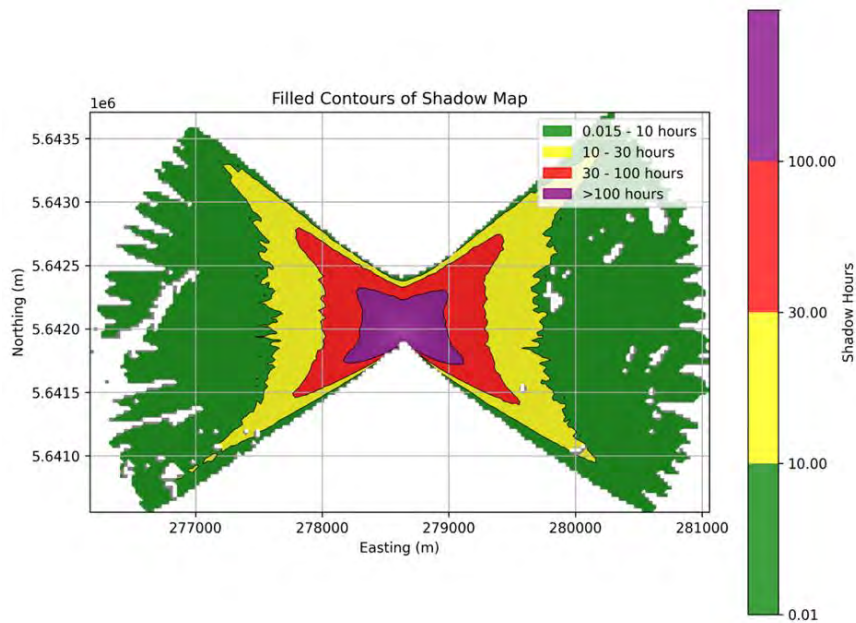


Figure 30 Contour map of shadow flicker frequency. A contour-based visualization of shadow flicker coverage, categorized into 10, 30, and 100-hour intervals, illustrates the extent and intensity of shadow flicker exposure.

Secondly, the choice of color made people associate it with “danger/bad” or “safe/good,” which could be misleading because we know that the probability of shadow flicker from modern turbines has direct health impacts on people (even those with photosensitive epilepsy) is non-existent. However, we know that people might get annoyed by shadow flicker and that annoyance can lead to stress, ultimately resulting in health issues. Therefore, to indicate that there is a potential impact and to account for the most widely adopted shadow flicker limit in European Union regulations, we use a single neutral color band, ranging from slate blue to lavender purple, to present the shadow flicker map with regions over 30 hours and over 0 hours (Figure 31). This 30-hour threshold also provides an intuitive reference, as it approximates one full day of shadow flicker per year.

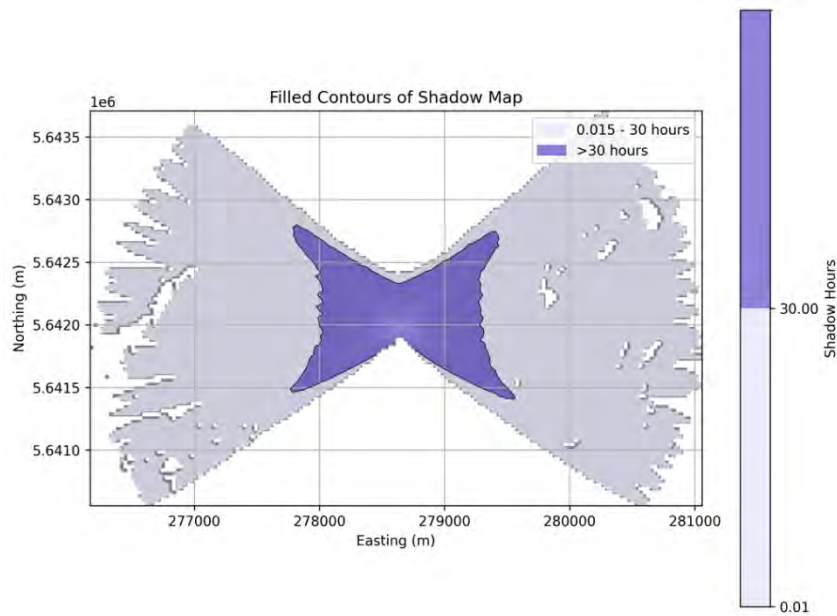


Figure 31 Binary Shadow Flicker Contour Map – A simplified contour representation of shadow flicker coverage, distinguishing between areas with less than 30 hours and greater than 30 hours of shadow flicker per year with single-color bands.



4. Accident risk assessment

The accident risk assessment builds upon the established framework developed by the Paul Scherrer Institute (PSI). For a concise overview, refer to the articles by Kim et al. (2018), Burgherr and Hirschberg (2014), and Spada and Burgherr (2023).

4.1 Updates and extensions since the intermediate version

Compared to the initial version of this deliverable, the following updates and enhancements have been developed and implemented for the accident risk assessment.

- i. The coverage of the accident database has been expanded until the end of 2023⁴.
- ii. The accident data has been linked to wind farm and wind turbine information from the Windpower Net Database, which PSI acquired during the WIMBY project. This data was also compared and cross-checked with the wind turbine database compiled by DTU as part of the WIMBY project.
- iii. The geographic location of each accident has been re-verified and linked to the NUTS (Nomenclature of Territorial Units for Statistics) classification⁵ used by the European Commission.
- iv. The accident risk indicators (i.e., fatality rates) have been disaggregated to the NUTS2 Level (i.e., «basic regions»).
- v. Furthermore, the consequences of accidents (i.e., fatalities and injuries) were converted into Disability-Adjusted Life Years (DALYs) and broken down in a manner similar to that of fatality rates.
- vi. A Bayesian Hierarchical Model (HBM) was created to compute country-specific DALY rates.
- vii. A map showing DALY rates was created using the QGIS software and published as *Geopackage* data files.

⁴ Data for 2024 have become available at the time of writing this report but could not be included in the present analysis due to time constraints.

⁵ <https://ec.europa.eu/eurostat/web/nuts>

Each of these steps is described in detail in the next section.

4.2 Overview of methodological approach

The methodological approach consists of three phases, which are outlined in the following sections.

4.2.1 Update of accidents database

The accident database established at the beginning of the project (refer to deliverable D2.2a and Burgherr et al. (2023))⁶ has been updated, cross-checked, and enriched with additional information.

- Accidents that occurred in 2023 have been added, following the same procedure described in the references mentioned above.
- Based on the available information collected from primary sources, the specific wind farm where the accident occurred, and the turbines involved were identified using the Windpower Net Database. A direct link was established with the accident database by using the wind farm ID from the Windpower Net Database. It was not possible to (semi-) automatically fetch this information for every accident. Therefore, a supplementary manual search was also conducted.
- Identifying the affected wind farm also facilitated the geo-referencing of the accidents. This was accomplished either through the coordinates provided in the Windpower Net Database or through a manual search using online resources⁷.
- Using QGIS software, the accident databases were joined with the NUTS classification system to assign each accident to various administrative units, namely NUTS0 (countries), NUTS1 («major socio-economic regions»), and NUTS2 («basic regions»).

⁶ Burgherr, Peter, Eleftherios Siskos, Russell McKenna, and Matteo Spada. 2023. "Comparative Risk Assessment of Wind Turbine Accidents from a Societal Perspective." In *Proceeding of the 33rd European Safety and Reliability Conference (ESREL 2023)*, edited by M.P. Brito, T. Aven, P. Baraldi, M. Cepin, and E. Zio. Singapore, SG: Research Publishing Services. https://rpsonline.com.sg/proceedings/esrel2023/pdf_proceeding/esrel2023-proceedings-fa.pdf.

⁷ Open Infrastructure Map: <https://openinframap.org>

The updated and extended accident database was the basis for the subsequent analyses.

4.2.2 Calculation of risk indicators

Aggregated indicators, such as fatality rates, are standard risk measures for comparing the performance of energy technologies concerning accidents. The current data set of accidents in the wind energy sector compiled during the WIMBY project has been analyzed, and results for fatality risks have been published in Burgherr et al. (2023).

In the first step, risk indicators were calculated for three country groups: the Organization for Economic Cooperation and Development (OECD), the European Union (EU27, excluding the UK), and non-OECD countries. This ensures a broad comparison of accident risks beyond EU27 as well as previously published results, and, furthermore, it allows additional insights on UK and EU candidate countries that otherwise would not be included. Additionally, fatality rates were normalized per unit of electricity generation (i.e., Gigawatt-electric-year, *GWeyr*) to ensure direct comparisons between country groups and the corresponding onshore and offshore accidents.

The update presented in this deliverable, therefore, focuses on disaggregating fatality rates to the NUTS2 level (see Chapter 4.1). To achieve this, a two-step approach was applied. In countries with a sufficient number of accidents, country-specific fatality rates were directly calculated. In cases where a country had no fatal accidents, the aggregated fatality rate for the EU27, European Free Trade Association (EFTA), or EU candidate countries⁸ was used as a proxy.

Subsequently, country fatality rates were further disaggregated to the NUTS2 level through capacity-based downscaling, which refers to the installed wind power capacity in Megawatts (MW) per NUTS2 unit of a country. This

⁸ Albania, Bosnia and Herzegovina, Kosovo, Montenegro, North Macedonia, Serbia, and Turkey were considered, whereas Georgia, Moldova and Ukraine were excluded.

follows the general ideas described in Hidalgo Gonzalez and Uihlein (2023)⁹. Data from the IRENASTAT¹⁰ tool of the International Renewable Energy Agency (IRENA) were utilized to normalize fatality rates per Gigawatt-electric-year (GWeyr), allowing for direct comparisons between geographic units. Fatality rates were computed for all fatal accidents (≥ 1 fatality), and severe fatality rates were also calculated, focusing exclusively on accidents with at least five fatalities (Burgherr et al., 2019)¹¹. The latter is an essential measure for comparing a diverse set of energy technologies (e.g., fossil, renewable, nuclear) (Burgherr and Hirschberg, 2014)¹².

4.2.3 Calculation of DALY and risk map

Accidents can lead to various consequences, including fatalities and injuries. Typically, these consequences are reported individually through normalized, aggregated risk indicators. Composite indicators that combine different impacts can enable broader comparisons across disciplines. Examples of accident risk assessment include:

- Value of Statistical Life (VSL) calculates external costs (Burgherr, Hirschberg, and Spada 2013)¹³.

⁹ Hidalgo Gonzalez, I., and A. Uihlein. 2023. "High-Resolution Energy Atlas. Methodology and Data." Luxembourg. <https://doi.org/https://dx.doi.org/10.2760/83784>.

¹⁰ <https://www.irena.org/Data/Downloads/IRENASTAT>

¹¹ Burgherr, Peter, Matteo Spada, Anna Kalinina, Laurent Vandepaer, Peter Lustenberger, and Wansub Kim. 2019. "Comparative Risk Assessment of Accidents in the Energy Sector within Different Long-Term Scenarios and Marginal Electricity Supply Mixes." In *Proceedings of the 29th European Safety and Reliability Conference, ESREL 2019*, 1525–32. https://doi.org/10.3850/978-981-11-2724-3_0674-cd.

¹² Burgherr, Peter, Hirschberg, Stefan. 2014. "Comparative Risk Assessment of Severe Accidents in the Energy Sector." *Energy Policy* 74 (December):S45–56. <https://doi.org/10.1016/j.enpol.2014.01.035>.

¹³ Burgherr, P., S. Hirschberg, and M. Spada. 2013. "Comparative Assessment of Accident Risks in the Energy Sector." In *Handbook of Risk Management in Energy Production and Trading. International Series in Operations Research and Management Science*. Vol. 199. New York, USA: Springer Science + Business Media. https://doi.org/10.1007/978-1-4614-9035-7_18.



- The comparison of the impacts from Life Cycle Assessment (LCA), Comparative Risk Assessment (CRA), and terrorist threat assessment based on Years of Life Lost (YOLL) (Hirschberg et al. 2016)¹⁴.
- The use of composite indicators in National Risk Assessment (NRA) focuses on aggregation through monetization (Spada, Burgherr, and Hohl 2019)¹⁵.

For this deliverable, we employ a method that utilizes Disability-Adjusted Life Years (DALY). This approach is based on a robust foundation established by the Global Burden of Disease (GBD) study¹⁶, which evaluates health losses due to diseases, injuries, and risk factors. Furthermore, it produces results that can be compared with estimates from other activities in WIMBY, such as LCA and noise assessment.

¹⁴ Hirschberg, S., C. Bauer, P. Burgherr, E. Cazzoli, T. Heck, M. Spada, and K. Treyer. 2016. "Health Effects of Technologies for Power Generation: Contributions from Normal Operation, Severe Accidents and Terrorist Threat." *Reliability Engineering and System Safety* 145. <https://doi.org/10.1016/j.ress.2015.09.013>.

¹⁵ Spada, M., and P. Burgherr. 2020. "A Hierarchical Approximate Bayesian Computation (HABC) for Accident Risk in the Energy Sector Triggered by Natural Events." In *Proceedings of the 29th European Safety and Reliability Conference, ESREL 2019*. <https://doi.org/10.3850/978-981-11-2724-30758-cd>.

¹⁶ <https://www.healthdata.org/research-analysis/gbd>

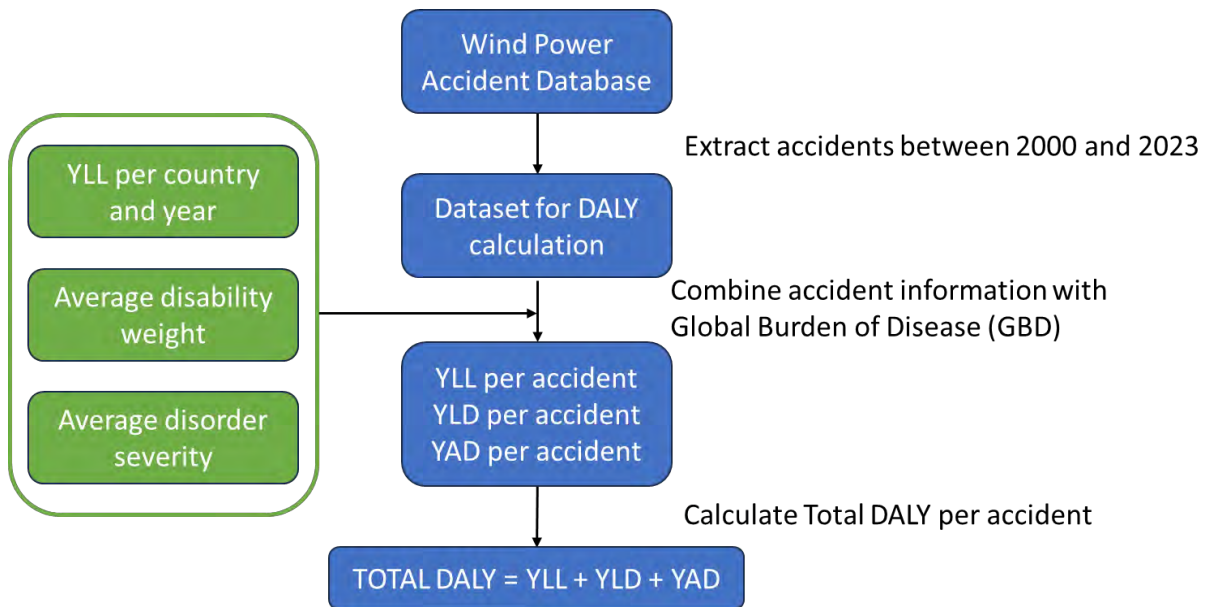


Figure 32: Approach to estimating Disability-Adjusted Life Years (DALY) for all accidents considered in the years 2000–2023 across European countries. YLL = Years of Life Lost, YLD = Years Lived with Disability, YAD = Years with Anxiety Disorder.

The proposed DALY calculation method for accident risk assessment is visualized in Figure 32 and involves the following steps:

Step 1: The complete wind power accident database is queried for accidents that occurred between 2000 and 2023. Further criteria include (i) the geographic area (Europe, including the EU, EFTA, and candidate countries as previously defined), (ii) accidents that are attributed to a specific location and event (excluding generic and summary reports), and (iii) onshore wind power (excluding offshore activities). This resulted in 1,243 accidents being considered in the subsequent DALY analysis from a total of 3455 accidents stored in the complete database.

Step 2: The Years of Life Lost (YLL) per country and year were estimated using data from the World Health Organization (WHO) and the International Labor Organization (ILO). The Global Health Observatory of the WHO provides data on life expectancy at birth, expressed in years, by country and year. The ILOSTAT database, provided by the ILO, offers information on the working-age population by sex and age (in thousands) for each country and year. The difference between the two values is considered an appropriate proxy for the years of life lost (YLL) due to fatalities in accidents. This simplification

aligns with the discussions of Hirschberg et al. (2016)¹⁷ and Spada and Burgherr (2021)¹⁸. This represents a conservative (maximum) estimate; however, the actual age of workers and/or public individuals affected by an accident is typically unknown, as it is not available in the existing reports. Nevertheless, this can be justified because wind power faces acceptance issues (McKenna et al., 2025)¹⁹. This approach addresses potential criticism that DALY estimates are on the lower end – a common argument raised in comparative risk assessments of accidents in the energy sector (Burgherr and Hirschberg 2014; 2008).

The Years Lived with Disability (YLD) estimates Disability-Adjusted Life Years (DALY) related to injuries. It is calculated by multiplying Years of Life Lost (YLL) with an average Disability Weight (DW) factor. Data obtained from the study «Disability Weights for the Global Burden of Disease 2013» (Salomon et al., 2015)²⁰ was utilized. Specifically, injury-related terms from Table 2 of this publication were selected, including "injury" and "musculoskeletal disorders." Terms associated with "untreated" or "without treatment" conditions were excluded. Of the 235 unique health states reported in this table, 37 were selected. The mean DW and 95% uncertainty interval were

¹⁷ Hirschberg, S., C. Bauer, P. Burgherr, E. Cazzoli, T. Heck, M. Spada, and K. Treyer. 2016. "Health Effects of Technologies for Power Generation: Contributions from Normal Operation, Severe Accidents and Terrorist Threat." *Reliability Engineering and System Safety* 145. <https://doi.org/10.1016/j.ress.2015.09.013>.

¹⁸ Spada, Matteo, and Peter Burgherr. 2021. "Comparative Risk Assessment and External Costs of Accidents for Passenger Transportation in Switzerland." In *Proceedings of the 31st European Safety and Reliability Conference (ESREL 2021)*, edited by Bruno Castanier, Marko Cepin, David Bigaud, and Christophe Berenguer. Singapore, SG: Research Publishing. <https://doi.org/10.3850/978-981-18-2016-8354-cd644>.

¹⁹ McKenna, Russell, Johan Lilliestam, Heidi U. Heinrichs, Jann Weinand, Johannes Schmidt, Iain Staffell, Andrea N. Hahmann, et al. 2025. "System Impacts of Wind Energy Developments: Key Research Challenges and Opportunities." *Joule* 9 (1): 101799. <https://doi.org/10.1016/j.joule.2024.11.016>.

²⁰ Salomon, Joshua A, Juanita A Haagsma, Adrian Davis, Charline Maertens de Noordhout, Suzanne Polinder, Arie H Havelaar, Alessandro Cassini, et al. 2015. "Disability Weights for the Global Burden of Disease 2013 Study." *The Lancet Global Health* 3 (11): e712–23. [https://doi.org/10.1016/S2214-109X\(15\)00069-8](https://doi.org/10.1016/S2214-109X(15)00069-8).



extracted for each state. The average of these 37 health states corresponds to a DW value of 0.16 (0.11 – 0.22). The YLD of an accident involving injuries is calculated by multiplying the country- and year-specific YLL by the average Disability Weight (DW).

The final part of the DALY calculation focuses on accidents that resulted in no fatalities or injuries. For these accidents, it is assumed that unique traumatic aspects may emerge, interacting with the varying perceptions of each individual involved, a topic that has been extensively researched among workers in high-risk environments (Carey et al. 2021)²¹. Similar to YLD, data from the Global Burden of Disease (GBD) study is presented in Table 1 of (Santomauro et al. 2023)²². An average Disability Weight (DW) is calculated for anxiety disorders, weighted by category (asymptomatic, mild, moderate, severe). Moreover, optimal treatment is assumed as the EU (including candidates) and the EFTA represent developed countries, with a duration not exceeding one year, as either the treatment is effective or a worker will not remain in the same role. The weighted anxiety disorder DW is valued at 0.06. Finally, based on an NREL study, we estimated the number of individuals working at a wind farm using a Full-Time Equivalent per Capacity (FTE/cap) relationship (Kotarbinski, Keyser, and Stefek 2020)²³.

The DALY associated with Years with Anxiety Disorder (YAD) for each accident corresponds to the following multiplication: wind farm capacity x FTE/cap x DW x duration (1 year).

²¹ Carey, Mary G., Cheryl Regehr, Shannon L. Wagner, Marc White, Lynn E. Alden, Nicholas Buys, Wayne Corneil, et al. 2021. "The Prevalence of PTSD, Major Depression and Anxiety Symptoms among High-Risk Public Transportation Workers." *International Archives of Occupational and Environmental Health* 94 (5): 867–75. <https://doi.org/10.1007/s00420-020-01631-5>.

²² Santomauro, Damian F, Caroline Purcell, Harvey A Whiteford, Alize J Ferrari, and Theo Vos. 2023. "Grading Disorder Severity and Averted Burden by Access to Treatment within the GBD Framework: A Case Study with Anxiety Disorders." *The Lancet Psychiatry* 10 (4): 272–81. [https://doi.org/10.1016/S2215-0366\(23\)00037-8](https://doi.org/10.1016/S2215-0366(23)00037-8).

²³ Kotarbinski, Matthew, David Keyser, and Jeremy Stefek. 2020. "Workforce and Economic Development Considerations from the Operations and Maintenance of Wind Power Plants. Technical Report NREL/TP-5000-76957." Golden, CO, USA. <https://www.nrel.gov/docs/fy21osti/76957.pdf>.

Step 3: Finally, the total DALY per accident equals the sum of YLL, YLD, and YAD. This procedure's output yielded a DALY estimate for every accident in the dataset, comprising 1243 accidents.

These DALY values are now utilized to calculate initial country-specific DALYs, which are subsequently downscaled to NUTS2 using the same capacity-based approach as described for fatality rates.

The entire dataset could be utilized for the DALY rather than just a portion, as was the case for fatalities. Consequently, a Bayesian Hierarchical Model (HBM) was developed, which offers several advantages compared to the direct calculation used for fatality rates. These advantages include (i) handling complex data structures (i.e., multiple levels), (ii) incorporating prior information (i.e., balancing sparse and noisy data), (iii) improving parameter estimation (i.e., borrowing strength across groups to yield more stable and accurate parameter estimates), (iv) uncertainty quantification (i.e., providing credible intervals in addition to point estimates), (v) flexibility (i.e., the ability to adapt models to a wide range of problems), and robustness to overfitting (i.e., models generalize better to new data). Bayesian models for risk assessment of energy accidents have been previously utilized, but not for the current issue of DALY estimation and geographic downscaling. Several recent publications offer further information on the technical implementation and application cases (Spada and Burgherr 2020²⁴; Kalinina, Spada, and Burgherr 2018²⁵). For further reading on Bayesian modeling, the reference book by Andrew Gelman is recommended (Gelman et al. 2003²⁶).

²⁴ Spada, M., and P. Burgherr. 2020. "A Hierarchical Approximate Bayesian Computation (HABC) for Accident Risk in the Energy Sector Triggered by Natural Events." In *Proceedings of the 29th European Safety and Reliability Conference, ESREL 2019*. <https://doi.org/10.3850/978-981-11-2724-30758-cd>.

²⁵ Kalinina, A., M. Spada, and P. Burgherr. 2018. "Application of a Bayesian Hierarchical Modeling for Risk Assessment of Accidents at Hydropower Dams." *Safety Science* 110. <https://doi.org/10.1016/j.ssci.2018.08.006>.

²⁶ Gelman, Andrew, John B. Carlin, Hal S. Stern, and Donald B. Rubin. 2003. *Bayesian Data Analysis*. Chapman and Hall/CRC. <https://doi.org/10.1201/9780429258480>.

The pseudocode below summarizes the HBM developed and applied in this study. It was written and executed using R version 4.4.3 and RStudio 2024.12.1 Build 563.

Start

1. Load necessary libraries
2. Load data from Excel file
3. Create a list of data for Stan
4. Define the Stan model
5. Choose the model type (i.e., Gaussian or lognormal) and fitting method (i.e., manual (set number of iterations and chains) or adaptive)
6. Fit the chosen model with the chosen fitting method
7. Check convergence diagnostics
8. Extract samples for country-specific parameters
9. Compute the mean and 95% credible intervals for each country, and the overall average of all countries
10. Create a data frame with the results
11. Print/Plot the results, and save to an Excel file
12. Print message indicating file has been saved

End

Two types of models have been included in the HBM: a Gaussian model and a lognormal model. The diagnostics revealed that the Gaussian model outperformed the lognormal model for the specified problem and dataset. In general, the code can be expanded to include additional model types and automatically test for the model with the best fit (e.g., based on information criteria such as the Akaike Information Criterion (AIC), Bayesian Information Criterion (BIC), Deviance Information Criterion (DIC), and Watanabe-Akaike Information Criterion (WAIC)).

The adaptive and manual selection of the number of iterations and chains in Bayesian models has its advantages and disadvantages. Adaptive selection can provide increased efficiency, improved mixing, and ease of use; however, it can also increase complexity and potentially introduce bias. Manual selection allows for full user control and transparency but is time-consuming and requires expertise. For the current analysis, we used a mixed approach to iteratively verify and enhance the manual settings.



Stan for R (accessed via the RStan package)²⁷, is a powerful tool/software that allows users to fit complex Bayesian models using the Stan programming language directly from R. The package provides functionalities for posterior inference, including sampling from posterior distributions using Markov Chain Monte Carlo (MCMC) methods. This integration makes it easier to perform advanced statistical analyses and model fitting within the R environment.

The BHM was separately applied to the subset of accidents with fatalities and/or injuries and the subset with no reported consequences due to their different characteristics and distributions.

In the next step, the country-specific DALY values were disaggregated to the NUTS2 level using the capacity scaling approach described before.

In the last step, a risk map was produced in QGIS. Desktop 3.83.3. For this purpose, several layers were selected and combined.

1. NUTS 1-3 layer, 2024 (source: GISCO data distribution)²⁸
2. Bosnia and Herzegovina was not included in the NUTS layer, so it was sourced from GADM²⁹
3. The United Kingdom uses after Brexit the International Territorial Level (ITL) Geography Hierarchy Boundaries available from the Open Geography Portal of the National Statistical Office³⁰
4. DALY values at the NUTS2 level were imported as an Excel file and then joined with the abovementioned shapefiles.
5. Locations of wind farm accidents were imported as a CSV file.
6. Individual wind turbine locations were provided as a CSV file by DTU. The data set is in the directory for internal WIMBY use in YODA.
7. OpenStreetMap was used as a standard background³¹

The generated DALY risk map was then stored as a GeoPackage data file, an open, standards-based format for storing geospatial data. This format

²⁷ <https://cran.r-project.org/web/packages/rstan/vignettes/rstan.html>

²⁸ <https://gisco-services.ec.europa.eu/distribution/v1/nuts-2024.html>

²⁹ <https://gadm.org/>

³⁰ <https://geoportal.statistics.gov.uk/>

³¹ <https://tile.openstreetmap.de/>

supports various spatial data types, including points, lines, polygons, and raster images, making it versatile for diverse geospatial applications. Additionally, GeoPackages data files are platform-independent and can be used across various software environments, enhancing interoperability and data sharing within the geospatial community³².

4.3 Results

The following sections present the main results concerning risk indicators and the DALY risk map.

4.3.1 Risk indicators

The complete data set comprises 1242 accidents at onshore wind farm facilities for the period 2000–2023, covering the European Union (EU), the United Kingdom (UK), the European Free Trade Association (EFTA), and EU candidate countries. Overall, 53 accidents resulted in fatalities, 63 in injuries, and 107 in casualties (i.e., fatalities and/or injuries).

Fatality risk indicators for country groups (i.e., OECD, EU27, and non-OECD countries) have already been published (Burgherr et al., 2023). Figure 33 presents an adapted version of the plot from this publication.

For all accidents with one or more fatalities, the performance of non-OECD countries is comparable to that of OECD and EU27, which contrasts with expectations (Burgherr and Hirschberg 2014³³). Possible explanations include the fact that large-scale capacity growth in non-OECD countries began later and that reporting in some countries may be less comprehensive, particularly regarding public information sources utilized in this study. Severe accidents, defined as those with five or more fatalities, exhibit the usual pattern. OECD and EU27 countries have lower fatality rates compared to non-OECD countries. This pattern may indicate differences in legal and regulatory frameworks, as well as organizational and

³² <https://www.geopackage.org/>

³³ Burgherr, Peter, Hirschberg, Stefan. 2014. "Comparative Risk Assessment of Severe Accidents in the Energy Sector." *Energy Policy* 74 (December):S45–56. <https://doi.org/10.1016/j.enpol.2014.01.035>.

management safety cultures, among the country groups (see Burgherr and Hirschberg, 2014³⁴ for a discussion and additional references).

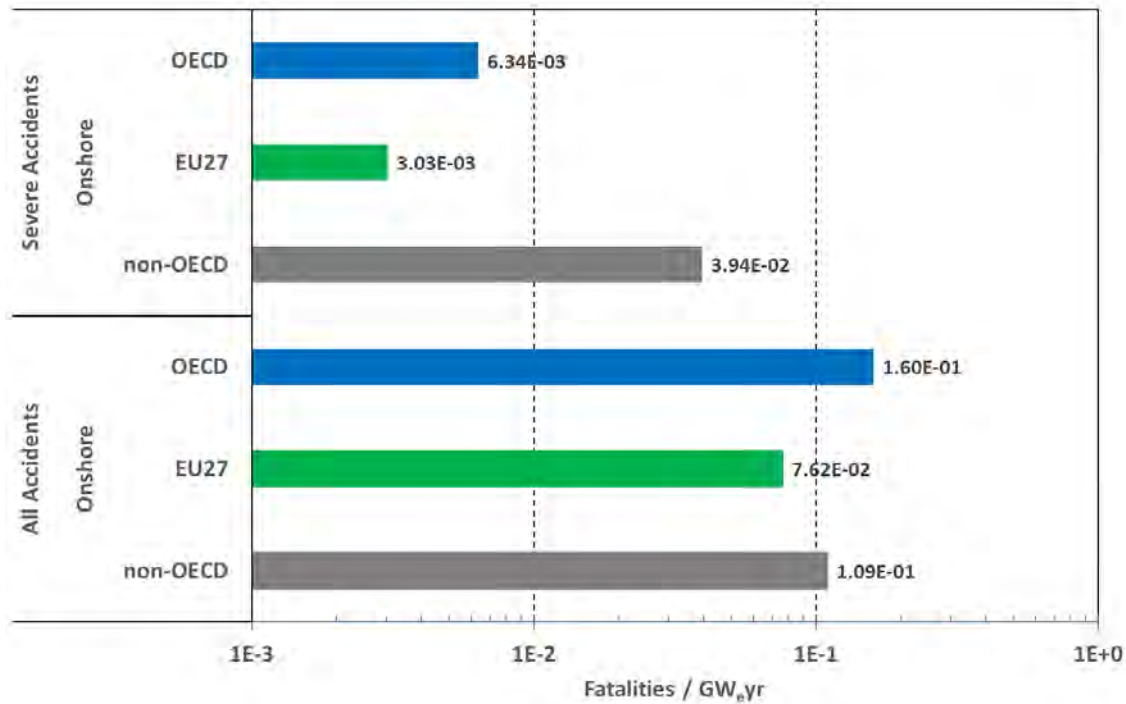


Figure 33: Onshore and offshore fatality rates for all accidents (with ≥1 fatality) and severe accidents (with ≥5 fatalities) in OECD, EU27, and non-OECD countries (adapted from Burgherr et al., 2023).

³⁴ Burgherr, Peter, Hirschberg, Stefan. 2014. "Comparative Risk Assessment of Severe Accidents in the Energy Sector." *Energy Policy* 74 (December):S45–56. <https://doi.org/10.1016/j.enpol.2014.01.035>.

The following discusses so-called fatality rates for severe accidents, ensuring that the data can be directly compared with other energy technologies (Burgherr and Hirschberg 2014³⁵; Burgherr et al. 2020³⁶; Spada and Burgherr 2023³⁷).

Similar to DALY rates, severe fatality rates were downscaled to the NUTS2 level, as previously described. Figure 34 presents the raw fatality rates per NUTS2 unit for the EU27, the UK, EFTA³⁸, and EU candidate countries³⁹. Compared to the EU, UK, and EFTA countries, the EU candidate countries exhibit substantially greater heterogeneity. This variation is due to limited data availability, lower data quality, and generally fewer activities in wind power development in these countries. Nevertheless, it was also decided to calculate fatality rates for these countries to provide order-of-magnitude estimates of how much they potentially still lag behind.

³⁵ Burgherr, Peter, Hirschberg, Stefan, 2014. "Comparative Risk Assessment of Severe Accidents in the Energy Sector." *Energy Policy* 74 (December):S45–56. <https://doi.org/10.1016/j.enpol.2014.01.035>.

³⁶ Burgherr, Peter, Matteo Spada, Laurent Vandepaer, Eleftherios Siskos, and Peter Lustenberger. 2020. "Risk-Benefits and Trade-Offs for a Broad Range of Long-Term Global Energy Scenarios." In *Proceedings of the 30th European Safety and Reliability Conference and the 15th Probabilistic Safety Assessment and Management Conference*, 5013. Venice, Italy: Research Publishing, Singapore. https://doi.org/10.3850/978-981-14-8593-0_4835-cd.

³⁷ Spada, Matteo, Burgherr, Peter. 2023. "Comparative Accident Risk Assessment of Energy System Technologies for the Energy Transition in OECD Countries." In *Proceedings of the 33rd European Safety and Reliability Conference*, edited by Mário P. Brito, Terje Aven, Piero Baraldi, Marko Čepin, and Enrico Zio. Singapore, SG: Rsearch Publishing.

³⁸ Iceland (IS), Liechtenstein (LS), Norway (NO), and Switzerland (CH).

³⁹ Albania (AL), Bosnia and Herzegovina (BI), Montenegro (ME), North Macedonia (MK), Serbia (RS), Turkey (TR), and Kosovo (XK).



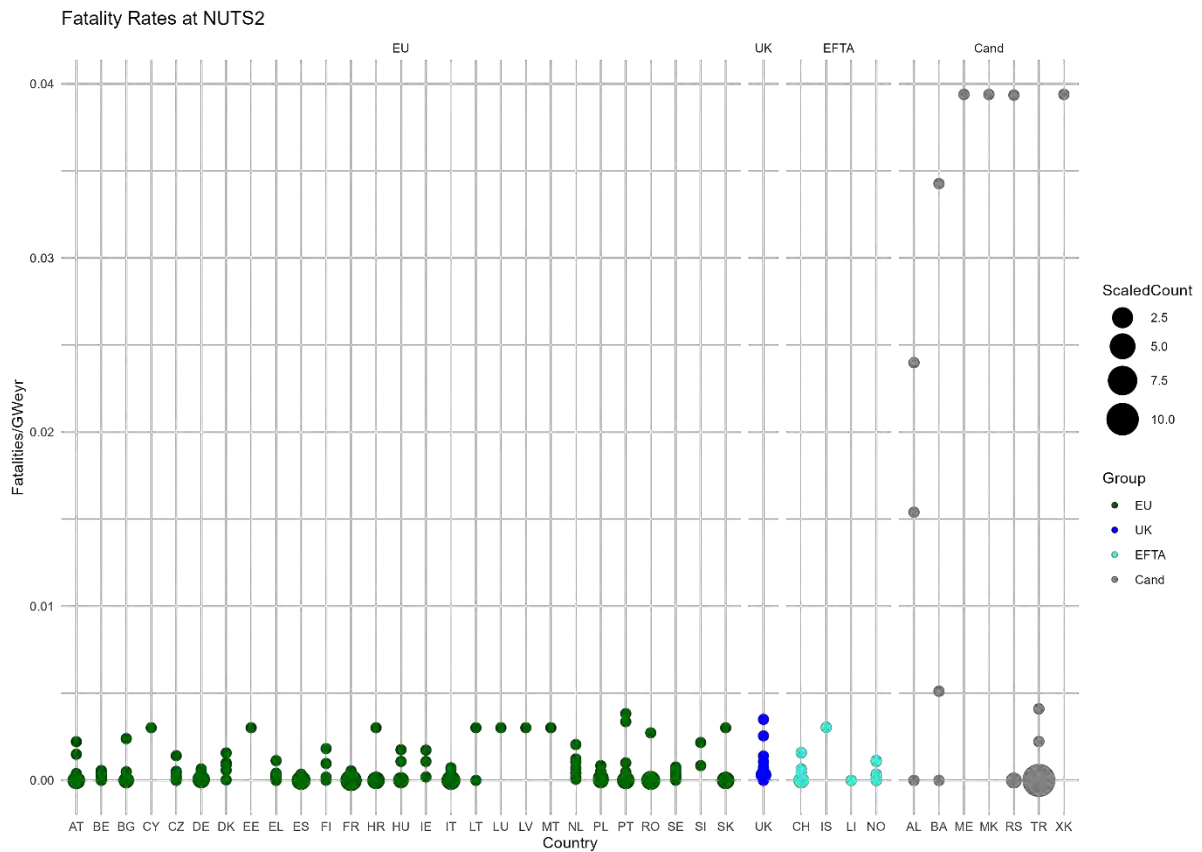


Figure 34: Raw fatality rates at NUTS2 level for EU27, UK, EFTA, and EU candidate countries, covering the period 2000–2023.

Comparing raw fatality rates is somewhat limited; therefore, average fatality rates and 95% confidence intervals were calculated for each country (Figure 35).

The average fatality rates for EU, UK, and EFTA countries are similar, while the rate for EU candidate countries is approximately one order of magnitude higher.

Within the EU, there are eight countries for which country- and NUTS-specific values could not be calculated. These countries are Cyprus (CY), Estonia (EE), Lithuania (LT), Latvia (LV), and Malta (MT), which each have only one NUTS2 region, as well as Croatia (HR), Luxembourg (LU), and Slovakia (SK), where all wind capacity is focused in a single NUTS region. Consequently, the average fatality rate for these countries matches the aggregated EU fatality rate (i.e., $3.03 \cdot 10^{-3}$ Fatalities/GW_e-year), reflecting a “base-case” fatality risk.

Moreover, these countries have minimal shares of onshore wind power in their electricity generation mix, resulting in relatively few accidents.

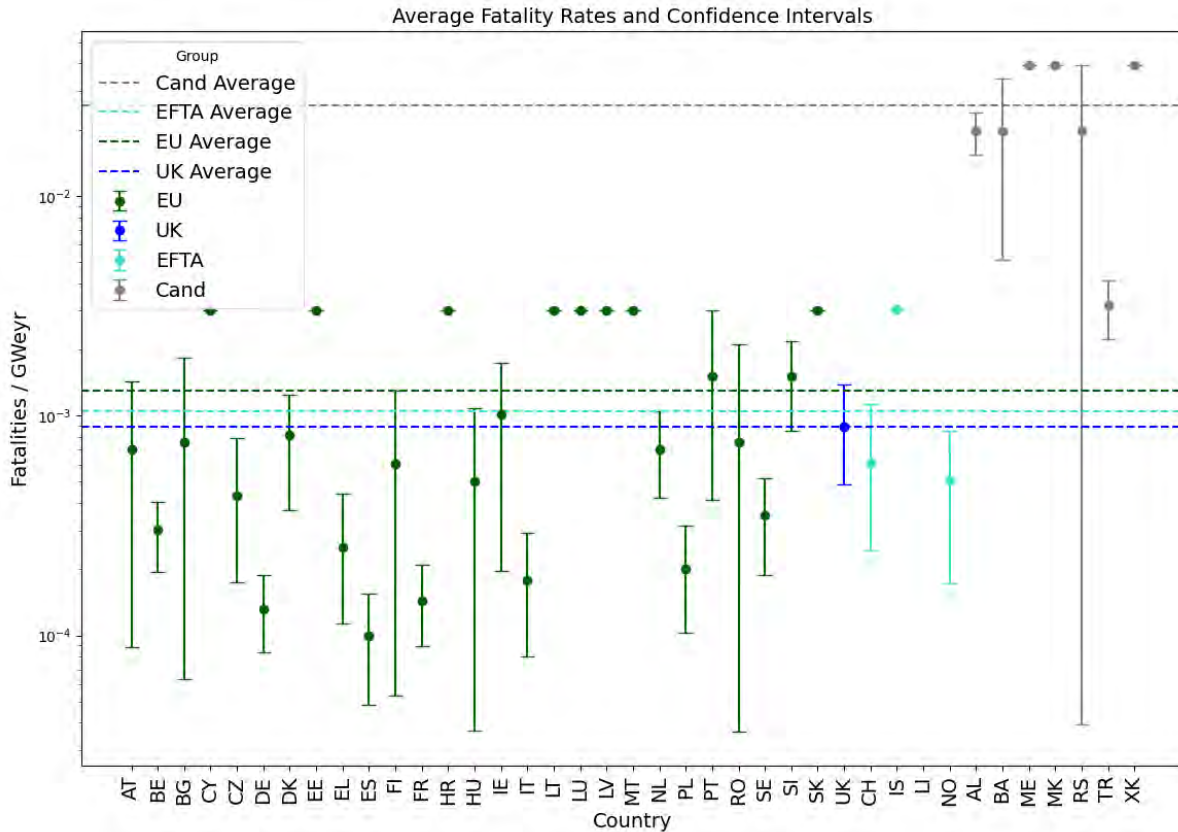


Figure 35: Average severe fatality rates and confidence intervals for each country, 2000-2023. Horizontal, dashed lines indicate average values per country group.

The other EU countries can be broadly categorized into three groups.

- Germany (DE), Spain (ES), France (FR), Italy (IT), Poland (PL), Greece (EL), Belgium (BE), and Sweden (SE) have the lowest average fatality rates and the narrowest confidence intervals (i.e., NUTS2 variability).
- Czechia (CZ), Hungary (HU), Finland (FI), the Netherlands (NL), Austria (AT), Bulgaria (BG), Romania (RO), and Denmark (DK). In this group, CZ, DK, and NL have significantly lower confidence intervals than the others, suggesting more accurate estimates. This implies that they belong to the lower half of the first group.
- Ireland (IE), Slovenia (SI), and Portugal (PT) are relatively close to the EU country average, yet they remain clearly below the aggregated EU fatality rate.

The UK and EFTA countries show a performance similar to that of the EU, comparable to the second group of EU countries, excluding Liechtenstein (LI)

and Iceland (IS). For Liechtenstein, no data is available for calculating the fatality rate; however, a performance similar to Switzerland may be anticipated as a first approximation. Similarly, the situation for Iceland mirrors that of the eight EU countries mentioned earlier. Therefore, Iceland is assigned the EFTA average fatality rate.

Among the group of EU candidates, only Turkey performs relatively close to the country-specific fatality rates of the other groups. However, available data for Turkey is limited and pertains only to a few NUTS units. For the other candidate countries, the situation is similar to that of the eight EU countries mentioned earlier (i.e., Montenegro, North Macedonia, and Kosovo), or the available data is limited (i.e., Albania, Bosnia and Herzegovina, and Serbia).

Despite this detailed discussion, it is crucial to emphasize and clarify several key aspects regarding the calculation of fatality rates at the NUTS2 level. All EU, UK, and EFTA countries have a country-specific average fatality rate that is below or, at most, equal to the aggregated EU fatality rate. Furthermore, EU, UK, and EFTA countries perform better than the OECD (see Figure 33). The EU candidate countries still align more closely with non-OECD countries than with OECD or even the EU, except for Turkey. Generally, the majority of wind farm accidents do not result in fatalities, and the maximum consequences of an accident are limited compared to other energy technologies (Burgherr and Hirschberg 2014⁴⁰). However, transparent and accurate reporting of accidental events, along with the calculation of consequences, remains necessary to provide objective information to stakeholders and the public, thereby balancing subjective perceived risks that may dominate the discussion. In the worst case, this can lead to decisions that are not fact-based, seek to please certain groups, and could even impede the overarching goals of the energy transition (McKenna et al. 2025⁴¹; Burgherr

⁴⁰ Burgherr, Peter, Hirschberg, Stefan. 2014. "Comparative Risk Assessment of Severe Accidents in the Energy Sector." *Energy Policy* 74 (December):S45–56. <https://doi.org/10.1016/j.enpol.2014.01.035>.

⁴¹ McKenna, Russell, Johan Lilliestam, Heidi U. Heinrichs, Jann Weinand, Johannes Schmidt, Iain Staffell, Andrea N. Hahmann, et al. 2025. "System Impacts of Wind Energy Developments:

et al. 2020⁴²). Finally, limited accident data regarding wind farm fatalities can result in significant uncertainties for some countries.

4.3.2 DALY risk map

The calculation of a risk indicator using Disability-Adjusted Life Years (DALY) offers several advantages. It can address issues related to limited data availability, provide a combined estimate of impacts (i.e., fatalities and injuries), and enable a direct comparison with other impacts (e.g., noise and LCA).

Consequently, the DALY risk indicator and the resulting risk map utilize the entire dataset of 1,242 wind farm accidents, following the methodology described in Chapter 4.3.1.

The map in Figure 36 clearly shows that only about 15% of all NUTS2 units fall into the two highest DALY categories (≥ 0.025), and less than one-third of them are classified in the top category. Even in the Nordic countries, Sweden and Norway have only two NUTS2 units each within the 0.1 – 0.75 category. Austria and Ireland are the other two countries with two NUTS2 units in this range.

At the opposite end of the scale, the three lowest DALY categories (≤ 0.001 DALY) account for nearly 30% of all NUTS units. Meanwhile, the proportion of the three intermediate NUTS2 categories is approximately the same, at about 33%.

Key Research Challenges and Opportunities.” *Joule* 9 (1): 101799. <https://doi.org/10.1016/j.joule.2024.11.016>.

⁴² Burgherr, Peter, Matteo Spada, Laurent Vandepaer, Eleftherios Siskos, and Peter Lustenberger. 2020. “Risk-Benefits and Trade-Offs for a Broad Range of Long-Term Global Energy Scenarios.” In *Proceedings of the 30th European Safety and Reliability Conference and the 15th Probabilistic Safety Assessment and Management Conference*, 5013. Venice, Italy: Research Publishing, Singapore. https://doi.org/10.3850/978-981-14-8593-0_4835-cd.



The NUTS2 units without DALY rates are mainly located in EU candidate countries such as Turkey, followed by nations in Eastern and Southeastern Europe.

Generally, the DALY rates exhibit similarities to the patterns observed in fatalities, particularly in countries where fatal accidents significantly impact populations. Conversely, high DALY rates may emerge in countries with a high volume of accidental events and/or numerous incidents involving injured individuals.

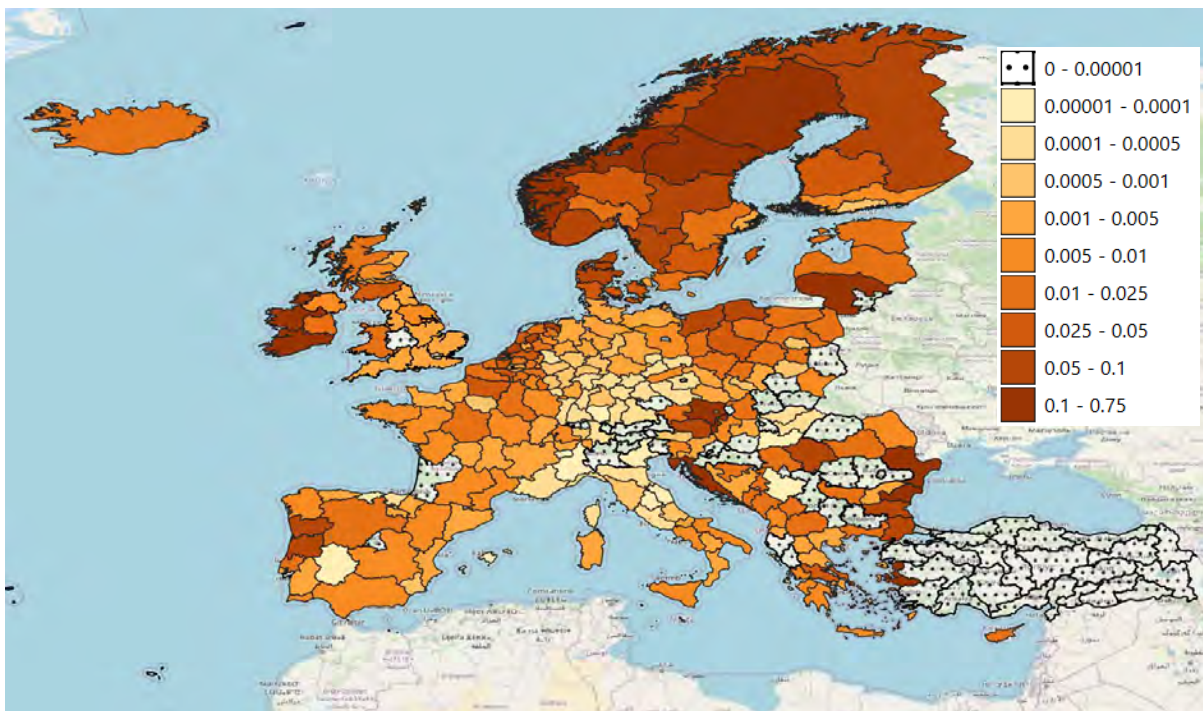


Figure 36: DALY rates (DALY = Disability-Adjusted Life Years) at the NUTS2 level for 38 European countries. NUTS2 units that feature a point pattern indicate that no DALY rates are available based on the current dataset.

The DALY values from wind farm accidents can be compared to the accidental impacts of other energy technologies, as well as the effects from

normal operations or intentional attacks (Hirschberg et al., 2016⁴³). However, Hirschberg and colleagues, in their study, considered only accidents that resulted in fatalities and did not convert the estimated Years of Life Lost into DALY. Similarly, the impacts during normal operations calculated in the WIMBY project, arising from noise and LCA, have not been converted to DALY. Nevertheless, our results suggest that the conclusion of the study by Hirschberg and colleagues, which states that the health impacts due to normal operations are much higher than those from accidents, is supported by our first-of-its-kind aggregate DALY estimates.

The DALY risk indicator map is available as a GeoPackage data file, as outlined in Chapter 4.2.3.

Future efforts could further enhance the estimation of health impacts expressed in DALY. More stringent and detailed reporting could reduce limitations in data availability and the number of assumptions required, ultimately leading to estimates with greater accuracy and lower uncertainties. However, this necessitates a collaborative effort from authorities, regulators, and industry, as it cannot be resolved by merely increasing the effort dedicated to the data collection process as a whole. From a methodological perspective, the applied methods and models could be enhanced by incorporating additional aspects and complexity. However, this partially depends on data quality and completeness; otherwise, the effects may not fully translate into the actual results.

Ultimately, a comparative perspective is essential. This applies to the considered technology portfolio (i.e., fossil fuels, large hydro, nuclear, and new renewables), the geographic scope (i.e., extending beyond Europe), and the potential future changes in health impacts from accidents (i.e., long-term energy transition scenarios).

⁴³ Hirschberg, S., C. Bauer, P. Burgherr, E. Cazzoli, T. Heck, M. Spada, and K. Treyer. 2016. "Health Effects of Technologies for Power Generation: Contributions from Normal Operation, Severe Accidents and Terrorist Threat." *Reliability Engineering and System Safety* 145. <https://doi.org/10.1016/j.ress.2015.09.013>.



5. Conclusions

The refined noise impact modeling framework presented in this deliverable marks a significant advancement in accurately representing wind turbine noise propagation. By adopting the updated ISO 9613-2:2024 standard—along with enhanced atmospheric attenuation modeling, ground and barrier effects, and the integration of ambient noise datasets—the tool now facilitates more detailed and realistic assessments of turbine-related sound impacts. These enhancements enable users to isolate the net noise contribution of wind turbines from other local sources, such as roads, railways, airports, and industrial facilities, thereby providing planners and stakeholders with a clearer understanding of the additional acoustic burden associated with wind energy development.

By leveraging detailed geospatial inputs, such as high-resolution elevation data and land cover information, the model captures localized terrain effects that can amplify or mitigate perceived noise levels. This improves the realism of the assessments and enables early identification of high-risk zones, supporting more proactive noise mitigation strategies and informed site selection. Future improvements will emphasize integrating additional environmental parameters, refining health impact quantification (e.g., DALYs per kWh), and expanding the validation dataset to further enhance model robustness and user confidence.

Concerning shadow flicker, the enhanced modeling approach represents a significant advancement in depicting turbine shadow projections across intricate terrains. The tool now integrates wind speed data to differentiate between operational and idle turbine states, yielding more realistic assessments compared to the worst-case scenario of constant operation. It also includes improved geometric calculations that factor in the Sun's angular diameter and penumbra effects, providing more precise estimates of flicker extent and intensity. The terrain-aware module modifies shadow projections based on topographic blocking and surface morphology, thus bringing model output into closer alignment with real-world conditions.

These methodological enhancements are validated through extensive testing with WindPRO—the leading industry standard software—and



demonstrate consistent performance across various European contexts. This ensures that the tool provides reliable, evidence-based insights to decision-makers and communities assessing potential shadow flicker exposure. The WIMBY tool is also fully open source.

The accident risk assessment provides detailed, spatially resolved indicators at the NUTS2 level. A novel method has been developed to compute Disability-Adjusted Life Years (DALY) as a comprehensive risk indicator, aggregating health impacts from both fatalities and injuries. Although the DALY risk map can already be integrated into the WIMBY interactive platform, future enhancements (beyond the scope of WIMBY)—outlined in Chapter 4.3.2—will be necessary to support higher-resolution calculations without introducing additional uncertainty through downscaling.

The computed indicators reveal significant geographic variability in accident-related health impacts. However, EU, UK, and EFTA countries generally display more favorable outcomes than the broader OECD group. These results also highlight that objective, data-driven indicators often contrast with subjective risk perceptions, which tend to overestimate actual impacts. Furthermore, the findings confirm that health risks from accidental events are minor compared to those associated with regular turbine operation (e.g., noise).

Overall, the methodologies and results presented in this deliverable enhance the WIMBY project's ability to support informed, equitable, and sustainable wind energy planning. As integration efforts continue under WP5, future work will build on the foundation established here—linking these models more directly with environmental policy tools, public communication interfaces, and region-specific energy transition strategies.



REFERENCES

- Bund-/Länder-Arbeitsgemeinschaft für Immissionsschutz (LAI). 2020. "Beurteilung Der Optischen Immissionen von Windenergieanlagen (Schattenwurf)."
- Burgherr, P., S. Hirschberg, and M. Spada. 2013. "Comparative Assessment of Accident Risks in the Energy Sector." In *Handbook of Risk Management in Energy Production and Trading. International Series in Operations Research and Management Science*. Vol. 199. New York, USA: Springer Science + Business Media. https://doi.org/10.1007/978-1-4614-9035-7_18.
- Burgherr, Peter, and Stefan Hirschberg. 2008. "A Comparative Analysis of Accident Risks in Fossil, Nuclear, and Hydro Energy Chains." *Human and Ecological Risk Assessment* 14:947–73. <https://doi.org/10.1080/10807030802387556>.
- . 2014. "Comparative Risk Assessment of Severe Accidents in the Energy Sector." *Energy Policy* 74 (December):S45–56. <https://doi.org/10.1016/j.enpol.2014.01.035>.
- Burgherr, Peter, Eleftherios Siskos, Russell McKenna, and Matteo Spada. 2023. "Comparative Risk Assessment of Wind Turbine Accidents from a Societal Perspective." In *Proceeding of the 33rd European Safety and Reliability Conference (ESREL 2023)*, edited by M.P. Brito, T. Aven, P. Baraldi, M. Cepin, and E. Zio. Singapore, SG: Research Publishing Services. https://rpsonline.com.sg/proceedings/esrel2023/pdf_proceeding/esre12023-proceedings-fa.pdf.
- Burgherr, Peter, Matteo Spada, Anna Kalinina, Laurent Vandepaer, Peter Lustenberger, and Wansub Kim. 2019. "Comparative Risk Assessment of Accidents in the Energy Sector within Different Long-Term Scenarios and Marginal Electricity Supply Mixes." In *Proceedings of the 29th European Safety and Reliability Conference, ESREL 2019*, 1525–32. https://doi.org/10.3850/978-981-11-2724-3_0674-cd.
- Burgherr, Peter, Matteo Spada, Laurent Vandepaer, Eleftherios Siskos, and Peter Lustenberger. 2020. "Risk-Benefits and Trade-Offs for a Broad Range of Long-Term Global Energy Scenarios." In *Proceedings of the 30th European Safety and Reliability Conference and the 15th Probabilistic Safety Assessment and Management Conference*, 5013. Venice, Italy: Research Publishing, Singapore. https://doi.org/10.3850/978-981-14-8593-0_4835-cd.



- Carey, Mary G., Cheryl Regehr, Shannon L. Wagner, Marc White, Lynn E. Alden, Nicholas Buys, Wayne Corneil, et al. 2021. "The Prevalence of PTSD, Major Depression and Anxiety Symptoms among High-Risk Public Transportation Workers." *International Archives of Occupational and Environmental Health* 94 (5): 867–75. <https://doi.org/10.1007/s00420-020-01631-5>.
- European Union. 2022. "COPERNICUS Digital Elevation Model (DEM) for Europe at 30 Meter Resolution Derived from Copernicus Global 30 Meter Dataset."
- Gelman, Andrew, John B. Carlin, Hal S. Stern, and Donald B. Rubin. 2003. *Bayesian Data Analysis*. Chapman and Hall/CRC. <https://doi.org/10.1201/9780429258480>.
- Hersbach, H., B. Bell, P. Berrisford, G. Biavati, Horányi A., Muñoz Sabater J., J. Nicolas, et al. 2023. "ERA5 Hourly Data on Single Levels from 1940 to Present." *Copernicus Climate Change Service (C3S) Climate Data Store (CDS)*, DOI: 10.24381/Cds.Adbb2d47147 (741): 4186–4227.
- Hidalgo Gonzalez, I., and A. Uihlein. 2023. "High-Resolution Energy Atlas. Methodology and Data." Luxembourg. <https://doi.org/https://dx.doi.org/10.2760/83784>.
- Hirschberg, S., C. Bauer, P. Burgherr, E. Cazzoli, T. Heck, M. Spada, and K. Treyer. 2016. "Health Effects of Technologies for Power Generation: Contributions from Normal Operation, Severe Accidents and Terrorist Threat." *Reliability Engineering and System Safety* 145. <https://doi.org/10.1016/j.res.2015.09.013>.
- International Organization for Standardization. 2024. "ISO 9613-2:2024 - Acoustics - Attenuation of Sound during Propagation Outdoors - Part 2: Engineering Method for the Prediction of Sound Pressure Levels Outdoors."
- ISO. 2010. "Acoustics - Attenuation of Sound During Propagation Outdoors - Part 1: Calculation of the Absorption of Sound By the Atmosphere." Vol. 1993.
- Kalinina, A., M. Spada, and P. Burgherr. 2018. "Application of a Bayesian Hierarchical Modeling for Risk Assessment of Accidents at Hydropower Dams." *Safety Science* 110. <https://doi.org/10.1016/j.ssci.2018.08.006>.
- Kim, Wansub, Peter Burgherr, Matteo Spada, Peter Lustenberger, Anna Kalinina, and Stefan Hirschberg. 2018. "Energy-Related Severe Accident



- Database (ENSAD): Cloud-Based Geospatial Platform." *Big Earth Data* 2 (4): 368–94. <https://doi.org/10.1080/20964471.2019.1586276>.
- Koppen, E., and M Ekelschot-Smink. 2023. "Standards for Regulating Environmental Impact of Wind Turbines." In *10th International Conference on Wind Turbine Noise*. Dublin, Ireland.
- Koppen, E., M. Gunuru, and A. Chester. 2017. "International Legislation and Regulations for Wind Turbine Shadow Flicker Impact." In *7th International Conference on Wind Turbine Noise*. Rotterdam, The Netherlands.
- Kotarbinski, Matthew, David Keyser, and Jeremy Stefek. 2020. "Workforce and Economic Development Considerations from the Operations and Maintenance of Wind Power Plants. Technical Report NREL/TP-5000-76957." Golden, CO, USA. <https://www.nrel.gov/docs/fy21osti/76957.pdf>.
- Länderausschuss für Immissionsschutz. 2002. "Hinweise Zur Ermittlung Und Beurteilung Der Optischen Immissionen von Windenergieanlagen (WEA-Schattenwurf-Hinweise)."
- McKenna, Russell, Johan Lilliestam, Heidi U. Heinrichs, Jann Weinand, Johannes Schmidt, Iain Staffell, Andrea N. Hahmann, et al. 2025. "System Impacts of Wind Energy Developments: Key Research Challenges and Opportunities." *Joule* 9 (1): 101799. <https://doi.org/10.1016/j.joule.2024.11.016>.
- Nagy, George. 1994. "Terrain Visibility." *Computers & Graphics* 18 (6): 763–73–773. [https://doi.org/10.1016/0097-8493\(94\)90002-7](https://doi.org/10.1016/0097-8493(94)90002-7).
- Salazar Trujillo, Jorge Hernán. 2014. "Calculation of the Shadow-Penumbra Relation and Its Application on Efficient Architectural Design." *Solar Energy* 110:139–50. <https://doi.org/10.1016/j.solener.2014.08.043>.
- Salomon, Joshua A, Juanita A Haagsma, Adrian Davis, Charline Maertens de Noordhout, Suzanne Polinder, Arie H Havelaar, Alessandro Cassini, et al. 2015. "Disability Weights for the Global Burden of Disease 2013 Study." *The Lancet Global Health* 3 (11): e712–23. [https://doi.org/10.1016/S2214-109X\(15\)00069-8](https://doi.org/10.1016/S2214-109X(15)00069-8).
- Santomauro, Damian F, Caroline Purcell, Harvey A Whiteford, Alize J Ferrari, and Theo Vos. 2023. "Grading Disorder Severity and Averted Burden by Access to Treatment within the GBD Framework: A Case Study with Anxiety Disorders." *The Lancet Psychiatry* 10 (4): 272–81. [https://doi.org/10.1016/S2215-0366\(23\)00037-8](https://doi.org/10.1016/S2215-0366(23)00037-8).
- Spada, M., and P. Burgherr. 2020. "A Hierarchical Approximate Bayesian Computation (HABC) for Accident Risk in the Energy Sector Triggered by





Natural Events.” In *Proceedings of the 29th European Safety and Reliability Conference, ESREL 2019*. <https://doi.org/10.3850/978-981-11-2724-30758-cd>.

Spada, Matteo, and Peter Burgherr. 2021. “Comparative Risk Assessment and External Costs of Accidents for Passenger Transportation in Switzerland.” In *Proceedings of the 31st European Safety and Reliability Conference (ESREL 2021)*, edited by Bruno Castanier, Marko Cepin, David Bigaud, and Christophe Berenguer. Singapore, SG: Research Publishing. <https://doi.org/10.3850/978-981-18-2016-8354-cd644>.

———. 2023. “Comparative Accident Risk Assessment of Energy System Technologies for the Energy Transition in OECD Countries.” In *Proceedings of the 33rd European Safety and Reliability Conference*, edited by Mário P. Brito, Terje Aven, Piero Baraldi, Marko Čepin, and Enrico Zio. Singapore, SG: Research Publishing.

Spada, Matteo, Peter Burgherr, and Markus Hohl. 2019. “Toward the Validation of a National Risk Assessment against Historical Observations Using a Bayesian Approach: Application to the Swiss Case.” *Journal of Risk Research* 22 (11): 1323–42. <https://doi.org/10.1080/13669877.2018.1459794>.

The European parliament. 2002. “Directive 2002/49/Ec.” *Official Journal of the European Communities*. Vol. L189.

